



LAWRENCE  
LIVERMORE  
NATIONAL  
LABORATORY

# Boundary Plasma Turbulence Simulations for Tokamaks

X.Q. Xu, M.V. Umansky, B. Dudson, P.B. Snyder

May 22, 2008

Communications in Computational Physics

## **Disclaimer**

---

This document was prepared as an account of work sponsored by an agency of the United States government. Neither the United States government nor Lawrence Livermore National Security, LLC, nor any of their employees makes any warranty, expressed or implied, or assumes any legal liability or responsibility for the accuracy, completeness, or usefulness of any information, apparatus, product, or process disclosed, or represents that its use would not infringe privately owned rights. Reference herein to any specific commercial product, process, or service by trade name, trademark, manufacturer, or otherwise does not necessarily constitute or imply its endorsement, recommendation, or favoring by the United States government or Lawrence Livermore National Security, LLC. The views and opinions of authors expressed herein do not necessarily state or reflect those of the United States government or Lawrence Livermore National Security, LLC, and shall not be used for advertising or product endorsement purposes.

# Boundary Plasma Turbulence Simulations for Tokamaks\*

X. Q. Xu<sup>1</sup>, M. V. Umansky<sup>1</sup>, B. Dudson<sup>2</sup>, and P. B. Snyder<sup>3</sup>

<sup>1</sup>*Lawrence Livermore National Laboratory, Livermore, CA 94550 USA*

<sup>2</sup>*University of York, Heslington, York YO10 5DD, UK*

<sup>3</sup>*General Atomics, San Diego, CA 92186 USA*

(Dated: May 15, 2008)

## Abstract

The boundary plasma turbulence code BOUT models tokamak boundary-plasma turbulence in a realistic divertor geometry using modified Braginskii equations for plasma vorticity, density ( $n_i$ ), electron and ion temperature ( $T_e, T_i$ ) and parallel momenta. The BOUT code solves for the plasma fluid equations in a three dimensional (3D) toroidal segment (or a toroidal wedge), including the region somewhat inside the separatrix and extending into the scrape-off layer; the private flux region is also included. In this paper, a description is given of the sophisticated physical models, innovative numerical algorithms, and modern software design used to simulate edge-plasmas in magnetic fusion energy devices. The BOUT code's unique capabilities and functionality are exemplified via simulations of the impact of plasma density on tokamak edge turbulence and blob dynamics.

PACS numbers: 52.55.Fa, 52.25.Fi, 52.30.Gz, 52.35.Ra, 52.65.Tt, 52.65.Kj, 52.65.-y

## Contents

<b>I. Introduction</b>	3
<b>II. BOUT Dynamical Equations</b>	7
A. BOUT plasma equations	7
B. Modified “parallel” viscous stress tensor $\overleftrightarrow{\pi}_{cj}$	10
C. Analytic neutrals model	11
D. Transformation of the electron parallel momentum equation	12
E. Simplification of vorticity	12
<b>III. Magnetic geometry</b>	13
A. Convention for magnetic field and its sign	13
B. The usual flux coordinates	14
C. Field-aligned coordinates	14
D. Twist-shift boundary conditions	16
E. Annular toroidal wedge	17
<b>IV. Spatial Numerical Implementations</b>	17
A. Radial derivatives in field-aligned coordinates	17
B. Inversion of the Laplacian operators	18
1. Inversion of potential vorticity	18
2. Inversion of $A_{\parallel}$	18
C. Numerical implementation of boundary conditions	19
1. Toroidal ( $z$ ) boundary conditions	19
2. Parallel ( $y$ ) boundary conditions	20
<b>V. Solving BOUT equations with PVODE</b>	23
<b>VI. BOUT Software Design</b>	24
<b>VII. BOUT Simulation Results</b>	26
A. Density effects on tokamak edge turbulence	27
B. Blob dynamics and correlation analysis	30

## VIII. Summary and Conclusions 33

### Acknowledgments 35

#### 1. Differential operators 35

a. Derivative along unperturbed magnetic field  $\vec{B}_0 \cdot \vec{\nabla}$  35

b. Laplacian  $\nabla_{\perp}^2$  35

c. Operator  $\vec{B} \times \vec{\nabla} \phi \cdot \vec{\nabla} A$  36

d. Operator  $\tilde{b} \cdot \vec{\nabla} G$  36

### References 36

## I. INTRODUCTION

The performance of tokamaks and other toroidal magnetic fusion devices depends crucially on the dynamics of the boundary region, i.e., the transition region from the hot core plasma through the separatrix to the material surface of the first wall, as shown in Fig. 1. Plasma turbulence, and the resulting anomalous cross-field plasma transport, are physical processes in the boundary region, affecting both core plasma confinement [e.g. high confinement mode (H-mode) and Edge Localized Modes (ELMs)], the density limit, and plasma-wall interactions [1]. The plasma boundary region has a number of physics attributes which make it quite distinct from the core: relatively low temperature, large radial gradients, and high neutral-gas and impurity densities, *proximity of open and closed flux surfaces, presence of X-point and sheath physics in the Scrape-Off-Layer (SOL)*. The large radial gradients tend to drive turbulent fluctuations which are a larger percentage of background values than in the core plasma.

Strong boundary turbulence has been observed in nearly all magnetic confinement devices [2]. There exist many experimental turbulence measurements in the pedestal region and in the SOL. Common diagnostics include electrostatic probes, reflectometry, phase contrast imaging (PCI), Beam Emission Spectroscopy (BES), and Gas Puff Imaging (GPI) [2]. Observed boundary turbulence has many common features, and a great deal of experimental data has been obtained over the past 20 years on e.g. fluctuation levels, spectra, correlation lengths, and scalings, but until recently this data could not be understood from first principles. The reason is simple. The diagnostics typically are limited either to local measurements in space

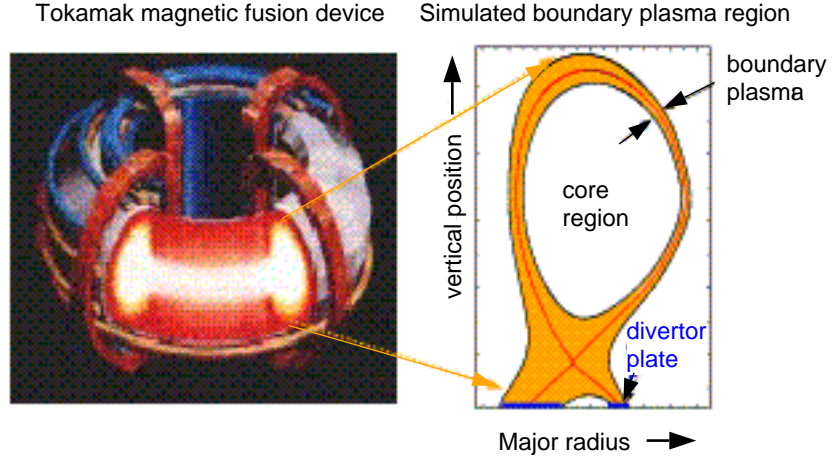


FIG. 1: Schematic views of tokamak and boundary plasma region (magnetic separatrix is red line).

or to particular turbulence quantities with certain working assumptions. Predictive simulation of boundary turbulence from fundamental physics models is therefore an important but daunting challenge owing to the special properties of the boundary plasma, its importance to an overall understanding of fusion plasmas, and the vast range of relevant spatial and temporal scales. A critical task is to demonstrate that simulations are able to reproduce the phenomena observed in real magnetic confinement devices. With the recent development of three dimensional (3D) non-linear codes, such as BOUT, it has become possible to make a direct computation of boundary turbulence, and validating these codes with experiments has since begun [3–8]. Using well bench-marked codes at the location of a particular measurement, boundary turbulence simulations are able to validate diagnostic tools and patch the experimental measurements together, yielding global understanding of boundary turbulence dynamics, and most importantly leading to scientific discoveries.

The BOUT code is a nonlinear initial-value two-fluid electromagnetic turbulence code in boundary plasmas that spans the separatrix [3, 9]. This 3-dimensional  $(\psi, \theta, \zeta)$  code represents configuration space via a grid in poloidal magnetic flux ( $\psi$ ), poloidal angle ( $\theta$ ) and toroidal angle ( $\zeta$ ). The geometry can be a circular annulus or that of a diverted tokamak and so includes boundary conditions for both closed magnetic flux surfaces and open field lines. The same set of fluid moment equations for plasma vorticity, density, ion and electron temperature and parallel momentum are discretized for both geometries. The equations are solved via a Method-of-Lines approach and an implicit backward-differencing scheme using

a Newton-Krylov iteration to advance the system in time via a fully implicit Newton-Krylov solver PVODE [10]. The spatial derivatives are discretized with finite differences. A fourth-order upwinding algorithm is used for nonlinear convections, and a second-order central difference scheme is used for the rest. Boundary conditions at conducting material surfaces are implemented on the plasma side of the sheath. The 3D BOUT code is parallelized based on a domain decomposition model by implementing message passing between multiple processors by using the MPI package [11]. In order to investigate boundary turbulence, BOUT is able to couple to the edge plasma transport code UEDGE [12], and MHD equilibrium code EFIT [13] and Corsica [14] to get the realistic X-point divertor magnetic geometry and plasma profiles.

BOUT contains much of the relevant physics for the edge barrier problem for the experimentally relevant X-point divertor geometry. The calculations were carried out to validate experimental measurements and simultaneously to provide consistent understanding of boundary turbulent dynamics. Encouraging results have been obtained when using measured plasma profiles in current generations of major fusion devices such as DIII-D, C-Mod and NSTX. The resistive X-point mode has been identified in X-point divertor geometry[3, 15]. Comparison of the shifted-circle vs. X-point geometry shows the different dominant modes and turbulence fluctuation levels[3]. The poloidal fluctuation phase velocity shows experimentally observed structure across the separatrix in many fusion devices[16]. The fluctuation phase velocity is larger than  $\mathbf{E} \times \mathbf{B}$  velocity. The Quasi-Coherent mode is believed to be responsible for the high energy confinement (H-mode), yet acceptably low particle (impurity) confinement in the Alcator C-Mod high density plasma regime. The experimentally measured dispersion and mode stability is in good agreement with the resistive ballooning X-point mode predicted by the BOUT code[17]. A strong poloidal asymmetry of particle flux in the proximity of the separatrix may explain the paradox of the JET probe measurement of the particle flux when comparisons of the limiter vs. divertor experiments had been made [16]. BOUT simulations performed with the measured discharge parameters show a Geodesic-Acoustic Mode (GAM) oscillation at the experimentally observed frequency [18]. Our L-H transition with simple sources added shows transitions with resistive X-point modes dominating L-mode and the levels of turbulence are similar to experimental measurements [16]. Blobs have also been clearly identified from BOUT runs and analysis of has shed insight on 3D X-point effects associated with increased convective velocity [19, 20]. X-point effects can

isolate blobs in the main SOL from divertor legs [21]. Simulations of C-MOD find blob-like structures with amplitudes and spatial correlation lengths comparable to those observed experimentally. BOUT simulations also provide evidence of instability and fluctuations in divertor legs that is uncorrelated with activity in the main SOL [22]. Simulations of Edge Localized Modes (ELMs) using the BOUT code find the expected peeling-ballooning mode structure and growth rates in the linear phase, followed by rapid radially outward propagation of filaments in the nonlinear phase [23]. Simulations of ELMs in DIII-D plasmas find a mode structure similar to that directly observed with fast cameras [23–25]

The BOUT project originally started in late 1990s to simulate boundary turbulence across the magnetic separatrix. The goal of the BOUT project is the development and deployment of a user-friendly, state-of-art, nonlinear fluid turbulence capability for the analysis of boundary turbulence in a general geometry on a routine basis. Since then, the BOUT code has been further developed with emphasis on readability of the source code, modularity in physics models, functionalities and/or macros for differential operators, consistency in higher-order spatial differencing, and finally thorough verifications via test problems [26]. The most recent development, BOUT++, is based on a object-oriented approach using language C++. The aim of BOUT++ is to automate the common tasks needed for simulation codes, and to separate the complicated (and error-prone) details such as differential geometry, parallel communication, and file input/output from the user-specified equations to be solved. Thus the equations being solved are made clear, and can be easily changed with only minimal knowledge of the inner workings of the code. As far as possible, this allows the user to concentrate on the physics, rather than worrying about the numerics [27].

A method for obtaining a self-consistent model of edge-plasma turbulence and long-time edge profile evolution has been explored by coupling 2D edge transport code UEDGE and 3D turbulence code BOUT via a relaxed iterative approach where each code is run on its own characteristic time scale. During each cycle of the iterative procedure, the toroidally averaged plasma profiles are evolved to steady state. A fraction of these profiles is used to update the profiles driving fluctuations in the 3D turbulence code. Likewise, a fractional update of the turbulent fluxes is provided to the transport code from the turbulence simulation [28]. The coupled transport/turbulence simulation technique provides a strategy to achieve physics-based predictions for future device performance.

The remainder of the paper is organized as follows. Section II presets physical models



for boundary turbulence and a set of BOUT dynamical equations. The magnetic geometry and BOUT field-aligned coordinates are described in Sec. III. The spatial numerical implementations is explained in Sec. IV. The background for understanding an implicit backward-differencing scheme using a Newton-Krylov iteration is presented in Sec. V. The brief description of BOUT software suite is given in Sec. VI. The sample BOUT simulations results are illustrated in Sec. VII. Finally, a summary of this paper is presented in Sec. VIII.

## II. BOUT DYNAMICAL EQUATIONS

### A. BOUT plasma equations

In the boundary plasma, the application of a fluid model is reasonable in part because of the low temperature and thus high collisionality along the magnetic field. Further, the dominant modes in our simulations are in the long-wavelength regime,  $k_{\perp}\rho_j \ll 1$ , so the perpendicular motion can also be described by a fluid approach. The small parameters to define the ordering are:  $\beta = 8\pi(p_j + p_e)/B^2 \ll 1$ ,  $\delta_j = \rho_j/L_{\perp} \sim k_{\perp}\rho_j \ll 1$ ,  $\Delta_j = \lambda_j/L_{\parallel} \sim k_{\parallel}\lambda_j \ll 1$ , and  $k_{\perp} \ll k_{\parallel}$ . Here  $k_{\perp}$  and  $k_{\parallel}$  are the components of the fluctuation wave vector perpendicular and parallel to magnetic field, respectively. As usual,  $p_j$  is pressure,  $\rho_j = v_{Ti}/\omega_{cj}$  is gyroradius, and  $\lambda_j = v_{Ti}/\nu_j$  is the mean-free path with  $v_{Ti} = \sqrt{2T_j/M_j}$ , the thermal speed,  $\omega_{cj}$  the gyrofrequency,  $\nu_j$  the characteristic collision frequency,  $T_j$  temperature,  $M_j$  mass for species  $j(j=i,e)$ . The magnitude of magnetic field is denoted by  $B$ . For application to micro-turbulence in tokamak edge transport barriers, an additional ordering  $\delta_v \equiv v/v_{th,i}$  is introduced: the ratio of plasma species flow velocities to ion thermal velocity. The short mean-free path description of magnetized plasma as originally formulated by Braginskii assumes a MHD ordering  $\delta_v \simeq 1$  [29], while Mikhailovskii and Tsypin first realized [30] and Simakov and Catto correctly derived [31] when a drift-ordering  $v \simeq v_{pi}$  is adopted,  $\delta_v \ll 1$  and the ion heat flux divided by ion density will be on the same order as the diamagnetic drift velocity  $v_{pi}$ . The end result is the “parallel” viscous stress tensor  $\overleftrightarrow{\pi}_{cj}$  being modified. Thus an appropriate set of equations to describe the turbulence is given by a seven-field model obtained by reduction of the Braginskii equations [3] in toroidal geometry based on drift-wave ordering with sources and sinks added:

$$\begin{aligned}
\frac{\partial V_{\parallel e}}{\partial t} + (\mathbf{V}_{\mathbf{E}} + V_{\parallel e} \mathbf{b}_0) \cdot \nabla V_{\parallel e} &= -\frac{e}{m_e} E_{\parallel} - \frac{1}{N_i m_e} (T_e \partial_{\parallel} N_i + 1.71 N_i \partial_{\parallel} T_e) \\
&+ 0.51 \nu_{ei} (V_{\parallel i} - V_{\parallel e}) \\
&- \frac{1}{N_i m_e} \frac{2}{3} B^{3/2} \partial_{\parallel} (B^{-3/2} \pi_{ce}), \\
&+ \frac{S_{\parallel e}^m}{N_i m_e} - \frac{S_e^{cx} + S_e^p}{N_i} V_{\parallel e},
\end{aligned} \tag{1}$$

$$\begin{aligned}
\frac{\partial \varpi}{\partial t} + (\mathbf{V}_{\mathbf{E}} + V_{\parallel i} \mathbf{b}_0) \cdot \nabla \varpi &= (2\omega_{ci}) \mathbf{b}_0 \times \kappa \cdot \left( \nabla P + \frac{1}{6} \nabla \pi_{ci} \right) \\
&+ N_i Z_i e \frac{4\pi V_A^2}{c^2} \nabla_{\parallel} j_{\parallel} + \mu_{ii} \nabla_{\perp}^2 \varpi \\
&- (B\omega_{ci}) \nabla \cdot \left( \frac{\mathbf{b}_0}{B} \times (\mathbf{S}_{\mathbf{e}}^m + \mathbf{S}_{\mathbf{i}}^m) \right) \\
&- \left( \frac{S_i^{cx}}{N_i} \right) \varpi - (\omega_{ci} B) \nabla \left( \frac{S_i^{cx}}{N_i \omega_{ci} B} \right) \cdot (N_i Z_i e \nabla \phi + \nabla P_i) \\
&- \frac{1}{2} \{ N_i Z_i e \mathbf{V}_{\mathbf{P}\mathbf{i}} \cdot \nabla (\nabla_{\perp}^2 \phi) - M_i \omega_{ci} \mathbf{b} \times \nabla N_i \cdot \nabla V_E^2 \} \\
&+ \frac{1}{2} \{ \mathbf{V}_{\mathbf{E}} \cdot \nabla (\nabla_{\perp}^2 P_i) - \nabla_{\perp}^2 (\mathbf{V}_{\mathbf{E}} \cdot \nabla P_i) \}
\end{aligned} \tag{2}$$

$$\begin{aligned}
\frac{\partial N_i}{\partial t} + (\mathbf{V}_{\mathbf{E}} + V_{\parallel i} \mathbf{b}_0) \cdot \nabla N_i &= \left( \frac{2c}{eB} \right) \mathbf{b}_0 \times \kappa \cdot (\nabla P_e - N_i e \nabla \phi) \\
&+ \nabla_{\parallel} \left( \frac{j_{\parallel}}{e} \right) - N_i \nabla_{\parallel} V_{\parallel i} + S_e^p,
\end{aligned} \tag{3}$$

$$\begin{aligned}
\frac{\partial T_i}{\partial t} + (\mathbf{V}_{\mathbf{E}} + V_{\parallel i} \mathbf{b}_0) \cdot \nabla T_i &= \frac{4}{3} \left( \frac{cT_i}{N_i e B} \right) \mathbf{b}_0 \times \kappa \cdot (\nabla P_e - N_i e \nabla \phi - \frac{5}{2} N_i \nabla T_i) \\
&+ \frac{2}{3N_i} \nabla_{\parallel} (\kappa_{\parallel i}^c \partial_{\parallel} T_i) \\
&- \frac{2T_i}{3N_i} \left( N_i \nabla_{\parallel} V_{\parallel i} - \frac{1}{e} \nabla_{\parallel} j_{\parallel} \right) + \frac{2}{3} \left( \frac{20}{3} \mu_{ii} \right) \nabla_{\perp}^2 T_i \\
&- \nu_I T_i + \left( \frac{2m_e}{M_i} \right) \frac{T_e - T_i}{\tau_e} + \frac{2S_i^E}{3N_i},
\end{aligned} \tag{4}$$

$$\begin{aligned}
\frac{\partial T_e}{\partial t} + (\mathbf{V}_{\mathbf{E}} + V_{\parallel e} \mathbf{b}_0) \cdot \nabla T_e &= \frac{4}{3} \left( \frac{cT_e}{N_i e B} \right) \mathbf{b}_0 \times \kappa \cdot \left( \nabla P_e - N_i e \nabla \phi + \frac{5}{2} N_i \nabla T_e \right) \\
&+ \frac{2}{3N_i} \nabla_{\parallel} (\kappa_{\parallel e}^c \partial_{\parallel} T_e) + \frac{2\eta_{\parallel}}{3N_i} j_{\parallel}^2 - \frac{2T_e}{3} \nabla_{\parallel} V_{\parallel e} + 0.71 \frac{2T_e}{3N_i e} \nabla_{\parallel} j_{\parallel} \\
&- \nu_I \left( T_e + \frac{2}{3} W_I \right) - \left( \frac{2m_e}{M_i} \right) \frac{T_e - T_i}{\tau_e} + \frac{2S_e^E}{3N_i},
\end{aligned} \tag{5}$$

$$\begin{aligned}
\frac{\partial V_{\parallel i}}{\partial t} + (\mathbf{V}_{\mathbf{E}} + V_{\parallel i} \mathbf{b}_0) \cdot \nabla V_{\parallel i} &= -\frac{1}{N_i M_i} \partial_{\parallel} P - \frac{2}{3} \frac{1}{N_i M_i} B^{3/2} \partial_{\parallel} (B^{-3/2} \pi_{ci}) \\
&+ \frac{S_{\parallel i}^m + S_{\parallel e}^m}{N_i M_i} - \frac{S_i^{cx} + S_i^p}{N_i} V_{\parallel i}.
\end{aligned} \tag{6}$$

Also, the auxiliary variables,  $\varpi$ ,  $\pi_{ci,e}$ , the parallel electric field, and the parallel Ampère's law are given by the following set of equations:

$$\nabla_{\perp}^2 A_{\parallel} = -\left(\frac{4\pi}{c}\right)j_{\parallel}, \quad (7)$$

$$E_{\parallel} = -\partial_{\parallel}\phi - \left(\frac{1}{c}\right)\frac{\partial A_{\parallel}}{\partial t}, \quad (8)$$

$$\varpi = N_i Z_i e \nabla_{\perp}^2 \phi + N_i Z_i e \nabla_{\perp} \phi \cdot \nabla_{\perp} \ln N_i + \nabla_{\perp}^2 P_i, \quad (9)$$

$$\begin{aligned} \pi_{ci,e} &\simeq (P_{\parallel} - P_{\perp})_{i,e} \\ &= \eta_{i,e}^0 \left( (\mathbf{V}_{\mathbf{E}} + \mathbf{V}_{\mathbf{Pi},e}) \cdot \boldsymbol{\kappa} - (2/\sqrt{B})\partial_{\parallel}(\sqrt{B}V_{\parallel i,e}) \right). \end{aligned} \quad (10)$$

Definitions of various quantities associated with plasma physics are as follows:

$$\begin{aligned} \mathbf{V}_{\mathbf{E}} &= c\mathbf{b}_0 \times \nabla_{\perp} \phi / B, \\ \mathbf{V}_{\mathbf{Pi},e} &= c\mathbf{b}_0 \times \nabla_{\perp} P_{i,e} / N_i Z_i e B, \\ \tilde{\mathbf{B}} &= \nabla A_{\parallel} \times \mathbf{b}_0, \\ \mu_{ii} &= \frac{3}{10} \nu_{ii} \rho_i^2, \\ \eta_i^0 &= 0.96 P_i \tau_i, \\ \eta_e^0 &= 0.73 P_e \tau_e, \\ \omega_{cj} &= \frac{Z_j e B}{M_j c}, \\ V_{Aj} &= \frac{B}{\sqrt{4\pi N_j M_j}}. \end{aligned}$$

Here  $\nabla_{\parallel} F = B \partial_{\parallel} (F/B)$  for any  $F$ ,  $\partial_{\parallel} = \partial_{\parallel}^0 + \tilde{\mathbf{b}} \cdot \nabla$ ,  $\tilde{\mathbf{b}} = \tilde{\mathbf{B}}/B$ ,  $\partial_{\parallel}^0 = \mathbf{b}_0 \cdot \nabla$ ,  $\boldsymbol{\kappa} = \mathbf{b}_0 \cdot \nabla \mathbf{b}_0$ . The symbol tilde represents the fluctuation quantities. Also,  $\mu_{ii}$ ,  $\mu_{\parallel}$ , and  $\chi_{\parallel}^c$  are the classical diffusion coefficients, and  $\nu_{ei}$  is electron collision frequency. Except for parallel viscous damping, magnetic pumping terms, and source and sink terms, similar equations are derived by Zeiler *et al.* [32]. Parallel electron viscous damping is important as it smoothes the high- $k_{\parallel}$  oscillations near the X-point. The ion temperature equation is important for proper determination of the fluctuating electric fields (because of the ion diamagnetic drift); also it may introduce the  $\eta_i$ -mode in the inner edge region [33, 34]. The last two terms in Eq. (2) are the lowest-order nonlinear convection terms after the gyroviscous cancellation in an expansion in inverse aspect ratio  $\epsilon = a/R$ .

Definitions of various quantities associated with neutrals are as follows:

$$\begin{aligned}
\nu_I &= N_n \langle \sigma v \rangle_I, \\
\nu_{cx} &= N_n \langle \sigma v \rangle_{cx}, \\
S^p &= N_i \nu_I, \\
S^{cx} &= N_i \nu_{cx}, \\
W_I &\simeq 20 eV.
\end{aligned}$$

Here  $\nu_I$  is the ionization rate,  $\nu_{cx}$  the charge exchange rate,  $W_I$  the average energy loss per ionization. The particle source term  $S^p$  arises from ionization of neutral gas and recombination and momentum source term  $S^{cx}$  arises from charge exchange. The external source terms are  $S^m$  for momentum,  $S^E$  for energy. In the derivation, it neglects ion momentum source/sink due to neutral.

## B. Modified “parallel” viscous stress tensor $\overleftrightarrow{\pi}_{cj}$

As we show in Ref. [35], the “parallel” viscous stress tensor  $\overleftrightarrow{\pi}_{cj}$  yields magnetic pumping term, which is important because it damps shear in the plasma flow. The turbulence fluctuation levels and transport are in turn regulated by the shear flow, via the time-varying  $E \times B$  flow shear de-correlation. However, the magnetic pumping term makes a negligible contribution to linear instability because it is on the order of  $\Delta_j$  smaller than other dominant linear curvature drives, such as the  $\nabla P$  term in Eq. (2).

Motivated by the observation for the importance of shear flow damping, the self-consistent expression for the ion “parallel” viscous stress tensor,  $\overleftrightarrow{\pi}_{cj}$ , is then carefully examined and is re-derived by Simakov and Catto in the drift-ordering as follows: [31]

$$\begin{aligned}
\pi_{cj} &= \eta_j^0 \left[ (\mathbf{V}_E + \mathbf{V}_{Pj}) \cdot \boldsymbol{\kappa} - \frac{2}{\sqrt{B}} \partial_{\parallel} (\sqrt{B} V_{\parallel j}) \right] \\
&+ \eta_j^0 \left[ \left( 1.61 c \frac{\mathbf{b} \times \nabla T_j}{Z_j e B} \right) \cdot \boldsymbol{\kappa} - \left( \frac{7.09}{5 p_j \sqrt{B}} \right) \partial_{\parallel} (\sqrt{B} q_{\parallel j}) \right] \\
&+ \eta_j^0 \left[ \left( \frac{2.44 q_{\parallel j}}{5 p_j} (2.27 \nabla_{\parallel} \ln T_j - \nabla_{\parallel} \ln p_j) \right) \right] \\
&- \eta_j^0 \left[ \left( \frac{4 \pi c}{B^3} \right) \mathbf{b} \times \nabla (p_i + p_e) \cdot \left( \nabla \phi + \frac{\nabla p_j}{Z_j e n} + 1.61 \frac{\nabla T_j}{Z_j e} \right) \right], \\
q_{\parallel i} &= -\kappa_{\parallel i} \nabla_{\parallel} T_i, \quad \kappa_{\parallel i} = \frac{125 p_i}{32 M_i \nu_i}.
\end{aligned} \tag{11}$$

In particular, this expression for  $\overleftrightarrow{\pi}_{cj}$  allows the neoclassical Pfirsch-Schlüter expression for  $V_{\parallel i}^{PS}$  to be recovered. Comparison with Eq. (10) for a MHD ordering shows the difference in last three-group terms.

### C. Analytic neutrals model

Fueling at the edge of a tokamak is a complex process and requires the use of fluid or Monte Carlo codes for the best available modeling. However, for purposes of examining the role of neutrals in pedestal density formation, it is reasonable to have an analytic neutrals model that includes sufficient physics to deal with the problem. One such model is a simple fluid neutral diffusion model where ion charge exchange (CX) gives rise to diffusion and ionization to the loss of neutrals. Since neutrals do not follow field lines, a simple neutral diffusion model can be setup from neutral continuity equation, with a radial coordinate  $r$  (for length in this case) to the wall,

$$\frac{\partial}{\partial r} \lambda_{CX} v_{th,n} \frac{\partial N_n}{\partial r} = N_n \nu_I. \quad (12)$$

where CX gives rise to diffusion as  $\Gamma_n \simeq -(T_n/M_n \nu_{cx}) \nabla N_n$  and ionization to the loss of neutrals. Here  $\nu_I = N_e \langle \sigma_{ion} v_{th,e} \rangle$ . This gives the well known results for the spatial distribution of neutrals:

$$N_n = N_w f(\theta) \exp \left( -\frac{r - r_w}{(\lambda_I \lambda_{cx})^{1/2}} \right). \quad (13)$$

where  $N_w$  is the neutral density at the main chamber wall and  $r_w$  is the position of the wall. The electron ionization and ion charge exchange lengths are, respectively,  $\lambda_I = v_{th,n}/\nu_I$ ,  $\lambda_{cx} = v_{th,n}/\nu_{cx}$ ,  $v_{th,n} = \sqrt{T_n/M_n}$ . Because the charge exchange collision frequency is often the largest, the gas and ion temperature are typically assumed equal, i.e.,  $T_n \simeq T_i$ . The model provides analytic expressions for the edge  $N_n$  profile in slab geometry with the assumption that the fueling is entirely from the plasma edge. A poloidally nonuniform source of neutrals is specified by  $f(\theta)$ . This simple model also allows the neutral density to adjust itself to plasma profile evolution via the electron ionization length  $\lambda_I$  and ion charge exchange length  $\lambda_{cx}$ . For a typical DIII-D L-mode plasma, the neutral density varies radially less than 30% from the wall to a few centimeters inside the last closed flux surface.

#### D. Transformation of the electron parallel momentum equation

Due to the time derivative in  $E_{||}$  of Eq. (8) in Eq. (1) one needs to introduce a new variable (canonical parallel momentum with an unity mass),

$$A_{j||} = V_{||e} - (e/m_e c)A_{||}, \quad (14)$$

to cast the equation in the form solvable by the method of lines. The parallel derivative is taken with respect to perturbed magnetic field

$$\partial_{||} = \vec{b} \cdot \nabla = \vec{b}_0 \cdot \nabla + \frac{\tilde{B}}{B} \cdot \nabla = \partial_{||}^0 + \frac{\nabla A_{||} \times \vec{b}_0}{B} \cdot \nabla \quad (15)$$

After combining time derivative and convection terms, the following equation

$$\frac{\partial V_{||e}}{\partial t} + \mathbf{V}_E \cdot \nabla V_{||e} = -\frac{e}{m_e} E_{||}, \quad (16)$$

leads to

$$\frac{\partial}{\partial t}(V_{||e} - \frac{e}{m_e c} A_{||}) + \mathbf{V}_E \cdot \nabla (V_{||e} - \frac{e}{m_e c} A_{||}) = \frac{e}{m_e} \partial_{||} \phi. \quad (17)$$

Denoting  $A_{j||} = V_{||e} - (e/m_e c)A_{||}$  and the original equation (1) can be rewritten as

$$\begin{aligned} \frac{\partial A_{j||}}{\partial t} + \vec{V}_E \cdot \nabla A_{j||} + V_{||e} \vec{b}_0 \cdot \nabla V_{||e} &= \frac{e}{m_e} \partial_{||}^0 \phi - \frac{1}{N_i m_e} (T_e \partial_{||} N_i + 1.71 n_e \partial_{||} T_e) + \\ 0.51 \nu_{ei} (V_{||i} - V_{||e}) - \frac{1}{N_i m_e} \frac{2}{3} B^{3/2} \partial_{||} (B^{-3/2} (P_{||e} - P_{\perp e})) &+ \frac{S_{||e}^m}{N_i m_e} - \frac{S_s^{cx} + S_e^p}{N_i} V_{||e} \end{aligned} \quad (18)$$

Accordingly Eq. (7) becomes the Helmholtz equation for the  $A_{||}$

$$\nabla_{\perp}^2 A_{||} - \frac{\omega_{pe}^2}{c^2} A_{||} = \frac{4\pi}{c} e N_i (A_{j||} - V_{||i}), \quad (19)$$

So solving it from given  $A_{j||}$  and  $V_{||i}$  one can find  $A_{||}$ , and then finds  $V_{||e}$ .

#### E. Simplification of vorticity

Vorticity is defined as

$$\varpi = N_i q \nabla_{\perp}^2 \phi + q \nabla_{\perp} \phi \cdot \nabla_{\perp} N_i + \nabla_{\perp}^2 P_i \quad (20)$$

Note that BOUT deals with perturbations of physical quantities, assuming that the zero order (equilibrium) terms cancel out altogether. The terms involving  $\nabla_{\perp} \phi_0$  and  $\nabla_{\perp} N_{i0}$  are dropped due to the large gradient scale length of equilibrium profiles. The nonlinear terms are dropped by an argument that this nonlinearity is not important for small fluctuations (e.g.  $N_i/N_{i0} \ll 1$ ). Then what is left is

$$\varpi = N_{i0} q \nabla_{\perp}^2 \phi + \nabla_{\perp}^2 P_i \quad (21)$$

Again,  $N_{i0}$  can be put under  $\nabla_{\perp}$  by same argument, and therefore the equation solved is

$$\nabla_{\perp}^2 \left( q \phi + \frac{P_i}{N_{i0}} \right) = \frac{\varpi}{N_{i0}} \quad (22)$$

### III. MAGNETIC GEOMETRY

#### A. Convention for magnetic field and its sign

In a axisymmetric toroidal system, the magnetic field can be expressed as

$$\mathbf{B} = I(\psi) \nabla \zeta + \nabla \zeta \times \nabla \psi, \quad (23)$$

where  $\psi$  is the poloidal flux,  $\theta$  is the poloidal angle-like coordinate, and  $\zeta$  is the toroidal angle. Here,  $I(\psi) = R B_t$ . The two important geometrical parameters are: the curvature,  $\kappa$ , and the local pitch,  $\nu(\psi, \theta) = I(\psi) \mathcal{J} / R^2$ . The local pitch  $\nu(\psi, \theta)$  is related to the MHD safety  $q$  by  $\hat{q}(\psi) = 2\pi^{-1} \oint \nu(\psi, \theta) d\theta$  in the closed flux surface region, and  $\hat{q}(\psi) = 2\pi^{-1} \int_{inboard}^{outboard} \nu(\psi, \theta) d\theta$  in the scrape-off-layer. Here  $\mathcal{J} = (\nabla \psi \times \nabla \theta \cdot \nabla \zeta)^{-1}$  is the coordinate Jacobian,  $R$  is the major radius, and  $Z$  is the vertical position.

In our notation  $\zeta$  is the geometric toroidal angle. Positive  $B_{\zeta}$  is in the  $\zeta$  direction, i.e. counter-clock-wise (looking from the top). For negative  $B_{\zeta}$ , which is considered the “normal” case, the ion  $\vec{\nabla} B$  drift is down [36]. For the poloidal component,  $B_{\theta}$ , the positive sign by convention corresponds to the direction from the inner plate to the outer one.

## B. The usual flux coordinates

For such an axisymmetric equilibrium the metric coefficients are only functions of  $\psi$  and  $\theta$ . Two spatial differential operators appear in the equations given as following:  $\nabla_{\parallel}$  and  $\nabla_{\perp}^2$ .

$$\nabla_{\parallel} = \mathbf{b}_0 \cdot \nabla = \frac{1}{\mathcal{J}B} \frac{\partial}{\partial \theta} + \frac{I}{BR^2} \frac{\partial}{\partial \zeta} = \frac{B_p}{hB} \frac{\partial}{\partial \theta} + \frac{B_t}{RB} \frac{\partial}{\partial \zeta}, \quad (24)$$

$$\nabla_{\perp}^2 \Phi = -\nabla \cdot [\mathbf{b} \times (\mathbf{b} \times \nabla \Phi)] = \nabla^2 \Phi - (\nabla \cdot \mathbf{b})(\mathbf{b} \cdot \nabla \Phi) - \nabla_{\parallel}^2. \quad (25)$$

If we use the usual flux coordinates  $(\psi, \theta, \zeta)$  and study the mode with

$$\rho_s \nabla_{\parallel} \simeq 0, \quad \rho_s \nabla_{\perp} \simeq 1,$$

since

$$\left| \rho_s \frac{B_p}{hB} \frac{\partial}{\partial \theta} \right| \simeq \left| \rho_s \frac{B_t}{RB} \frac{\partial}{\partial \zeta} \right| \simeq 1,$$

$\nabla_{\parallel} \simeq 0$  depends on the difference of two large and almost equal number, and therefore it is difficult to obtain accurate numerical solutions.

## C. Field-aligned coordinates

In order to efficiently simulate turbulence with short perpendicular wavelengths  $k_{\parallel} \ll k_{\perp}$ , we choose field-aligned coordinates[3, 37–39],  $(x, y, z)$ , which are related to the usual flux coordinates  $(\psi, \theta, \zeta)$  by the relations

$$\begin{aligned} x &= \psi - \psi_s, \\ y &= \theta, \\ z &= \zeta - \int_{\theta_0}^{\theta} \nu(x, y) dy. \end{aligned} \quad (26)$$

In the field-aligned coordinates, the parallel differential operator is simple, involving only one coordinate  $y$

$$\partial_{\parallel}^0 = \mathbf{b}_0 \cdot \nabla_{\parallel} = \left( \frac{B_p}{hB} \right) \frac{\partial}{\partial y} = \mathcal{J}_{\parallel} \frac{\partial}{\partial y}. \quad (27)$$

which requires a few grid points. However, magnetic shear leads to strong deformation of coordinate cells in the plane perpendicular to the field, and spatial discretization of radial derivative has to be taken care with special methods [3, 37, 38]. To remedy this we introduce a radial difference procedure in dual sets of coordinate systems. Even though the simulation



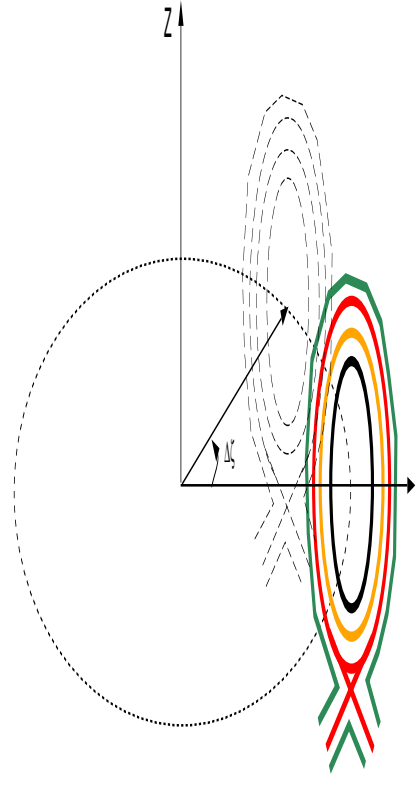


FIG. 2: (a) A sketch of the field-aligned coordinates mapping from  $(\theta, \zeta)$  to  $(y, z)$ . The area covered by the square ABCD is for the usual flux coordinates  $(\psi, \theta, \zeta)$ . The area covered by parallelogram ABEF is for the field-aligned coordinates  $(x, y, z)$ . The green area covered by the parallelogram  $AB_1E_1F$  is a truncated simulation domain by the name of an annular toroidal wedge; (b) A sketch of a annular toroidal wedge. The width of the wedge  $\Delta\zeta = 2\pi/\Delta n$ , where  $\Delta n \geq 1$  is an integer.

data resides on the field-aligned coordinates, the radial difference will be computed in the usual flux  $(\psi, \theta, \zeta)$  coordinates. Thus a high order interpolation scheme is needed to map data back and forth between the field-aligned coordinates and the usual flux  $(\psi, \theta, \zeta)$  coordinates. The derivatives are obtained from the chain rule as follows:

$$\frac{d}{d\psi} = \frac{\partial}{\partial x} - I \frac{\partial}{\partial z}, \quad (28)$$

$$\frac{d}{d\theta} = \frac{\partial}{\partial y} - \nu(x, y) \frac{\partial}{\partial z}, \quad (29)$$

$$\frac{d}{d\zeta} = \frac{\partial}{\partial z}, \quad (30)$$

$$I = \left( \int_{y_0}^y \frac{\partial \nu(x, y)}{\partial \psi} dy \right). \quad (31)$$

The coordinate Jacobian and metric coefficients are defined as following:

$$\mathcal{J} = (\nabla\psi \times \nabla\theta \cdot \nabla\zeta)^{-1} = \frac{h}{B_p}, \quad (32)$$

$$h = \sqrt{Z_\theta^2 + R_\theta^2}, \quad (33)$$

$$\mathcal{J}_{11} = |\nabla x|^2 = \frac{R^2}{\mathcal{J}^2}(Z_\theta^2 + R_\theta^2), \quad (34)$$

$$\mathcal{J}_{12} = \mathcal{J}_{21} = \nabla x \cdot \nabla y = -\frac{R^2}{\mathcal{J}^2}(Z_\theta Z_\psi + R_\psi R_\theta), \quad (35)$$

$$\mathcal{J}_{22} = |\nabla y|^2 = \frac{R^2}{\mathcal{J}^2}(Z_\psi^2 + R_\psi^2), \quad (36)$$

$$\mathcal{J}_{33} = \frac{1}{R^2}, \quad (37)$$

$$\mathcal{J}_\parallel = \frac{B_p}{hB}. \quad (38)$$

Here  $h$  is the local minor radius, and  $y_0$  is an arbitrary integration parameter. The disadvantage of this choice of coordinates is that the Jacobian diverges near the X-point as  $B_p \rightarrow 0$ . Therefore a better set of coordinates is needed for X-point divertor geometry.

#### D. Twist-shift boundary conditions

In the field-aligned coordinates the  $y$  coordinate is no longer periodic, but pseudo-periodic, because it is the coordinate along the field line and it carries with it a toroidal displacement in the binormal direction  $z$ . Therefore the twist-shift boundary conditions are applied in the poloidal direction inside the separatrix and periodic boundary conditions are applied in the binormal/toroidal direction:

$$f(\psi, \theta + 2\pi, \zeta) = f(\psi, \theta, \zeta) \longrightarrow f\left(x, y + 2\pi, z - \oint \nu dy\right) = f(x, y, z), \quad (39)$$

$$f(\psi, \theta, \zeta + 2\pi) = f(\psi, \theta, \zeta) \longrightarrow f(x, y, z + 2\pi) = f(x, y, z). \quad (40)$$

where the integral  $\oint \nu(x, y)dy$  represents a global shift by the periodicity constraint in the field-aligning transformation. If the simulation domain is the entire flux surface (the parallelogram ABEF in Fig. 2,  $0 \leq y \leq 2\pi, 0 \leq z \leq 2\pi$ ), the complete set of the Fourier modes  $n$  and  $m$  are kept.

### E. Annular toroidal wedge

For efficient simulations of turbulence with the high toroidal mode number  $n$  ( $n \gg 1$ ), in best practice a truncated computational domain on the full torus down to a toroidal wedge (the parallelogram  $AB_1E_1F$ ) is generally used, as shown in Fig. 2. To ensure the toroidal periodicity, the full torus has to be divided into an integer  $\Delta n$  equal parts (toroidal wedges) and enforce periodicity on each of them. However, after one poloidal cycle along the field line, the end of the field line is shifted by a global pitch  $\Delta\zeta \equiv \oint \nu(\psi, \theta) dy$ , in general it may fall into a different but an identical toroidal wedge, so the poloidal periodicity must be enforced after each such cycle. The periodic boundary conditions in a annular toroidal wedge then become:

$$f(\psi, \theta, \zeta + 2\pi) = f(\psi, \theta, \zeta) \longrightarrow f(x, y, z + 2\pi/\Delta n) = f(x, y, z), \quad (41)$$

$$f(\psi, \theta + 2\pi, \zeta) = f(\psi, \theta, \zeta) \longrightarrow f\left(x, y + 2\pi, z - \oint \nu dy\right) = f(x, y, z). \quad (42)$$

where  $\Delta n$  is a quantization constant, an integer. The consequence of the truncation of the computational domain is that the complete set of the  $n$ -spectrum is thinned from  $n = (0, \pm 1, \pm 2, \dots)$  to  $n = (0, \pm 1\Delta n, \pm 2\Delta n, \dots)$  in simulations of a annular toroidal wedge.

## IV. SPATIAL NUMERICAL IMPLEMENTATIONS

### A. Radial derivatives in field-aligned coordinates

According to the chain rule, the transformation of the radial derivative in field-aligned coordinates is given in Eq. (28). Due to the magnetic shear, the coordinate cell deformation occurs: a rectangle cell ( $\Delta\psi \sim \Delta\zeta$ ) in the flux coordinate becomes elongated in field-aligned coordinates  $\Delta x \gg \Delta z$  by a factor of  $I$  due to secular poloidal displacement of the two field lines, as shown in Fig. 3. The best way to handle this is to use finite Fourier transforms which is exact up to machine accuracy. Applying Fourier transform in  $z$  leads to

$$\frac{d}{d\psi} f_{kz}(x, y) = \frac{\partial}{\partial x} f_{kz}(x, y) - (ik_z I) f_{kz}(x, y), \quad (43)$$

where  $I$  is defined in Eq. (31) and can be pre-computed from magnetic geometry. However a preferred method is to (1) shift the Fourier transformed variable by a phase factor  $\exp[-ik_z \int_{y_0}^y \nu(\psi, y) dy]$ , and then (2) perform a finite difference on the transformed variable

$f_{kz}(x, y) \exp[-ik_z \int_{y_0}^y \nu(\psi, y) dy]$  in the usual flux coordinates where there is no cell deformation. Even though theoretically they are identical when  $\Delta\psi \rightarrow 0$ , this method has a advantage for a consistency in numerical approximations to match the twist-shifted boundary condition at the branch cut due to finite radial grid spacing  $\Delta\psi$  as following:

$$\begin{aligned} \mathcal{I}_{kz} &\equiv \frac{d}{d\psi} \exp \left[ -ik_z \int_{y_0}^y \nu(\psi, y) dy \right] \\ &\simeq \frac{\exp[-ik_z \int_{y_0}^y \nu(\psi + \Delta\psi, y) dy] - \exp[-ik_z \int_{y_0}^y \nu(\psi, y) dy]}{\Delta\psi} \\ &\xrightarrow{\Delta\psi \rightarrow 0} -ik_z I. \end{aligned} \quad (44)$$

In other words, the variable  $-ik_z I$  in Eq. (43) should be numerically pre-computed as one complex variable  $\mathcal{I}_{kz}$  defined as in Eq. (44), instead of as  $(-ik_z)$  times  $I$ .

## B. Inversion of the Laplacian operators

### 1. Inversion of potential vorticity

The vorticity equation is defined in Eq. (22). Using  $f \equiv Z_i e\phi + P_i/N_{i0}$  and the differential operator given in the Appendix (A4), and applying Fourier transform in  $z$  leads to

$$(RB_\theta)^2 \left\{ \frac{\partial^2 f_{kz}}{\partial x^2} + 2\mathcal{I}_{kz} \frac{\partial f_{kz}}{\partial x} + \left[ \mathcal{I}_{kz}^2 - k_z^2 \frac{B^2}{(RB_\theta)^4} \right] f_{kz} \right\} = \frac{\varpi_k}{\hat{N}_{i0}} \quad (45)$$

Here  $\mathcal{I}_{kz}$  is defined in Eq. (44). Solving the ordinary differential equation (ODE) using a tridiagonal linear solver yields  $f_{kz}(x, y)$ , then inverse Fourier transform yields  $f(x, y, z)$  in the field-aligned coordinates, from the latter  $Z_i e\phi = f(x, y, z) - P_i/N_{i0}$ . Note that in this procedure the radial boundary conditions for  $N_i, T_i$ , and  $\phi$  become linked together.

### 2. Inversion of $A_{||}$

Similarly, the Helmholtz equation for  $A_{||}$  from Eq. (19) in Fourier space can be written as

$$\begin{aligned} (RB_\theta) \left\{ \frac{\partial^2 A_{||kz}}{\partial x^2} + 2\mathcal{I}_{kz} \frac{\partial A_{||kz}}{\partial x} + \left[ \mathcal{I}_{kz}^2 - k_z^2 \frac{B^2}{(RB_\theta)^4} \right] A_{||kz} - \frac{\omega_{pe}^2}{c^2} A_{||kz} \right\} \\ = \frac{4\pi}{c} N_{i0} Z_i e (A_{j||} - V_{||i})_{kz} \end{aligned} \quad (46)$$

The solution procedure is same as that for the vorticity.

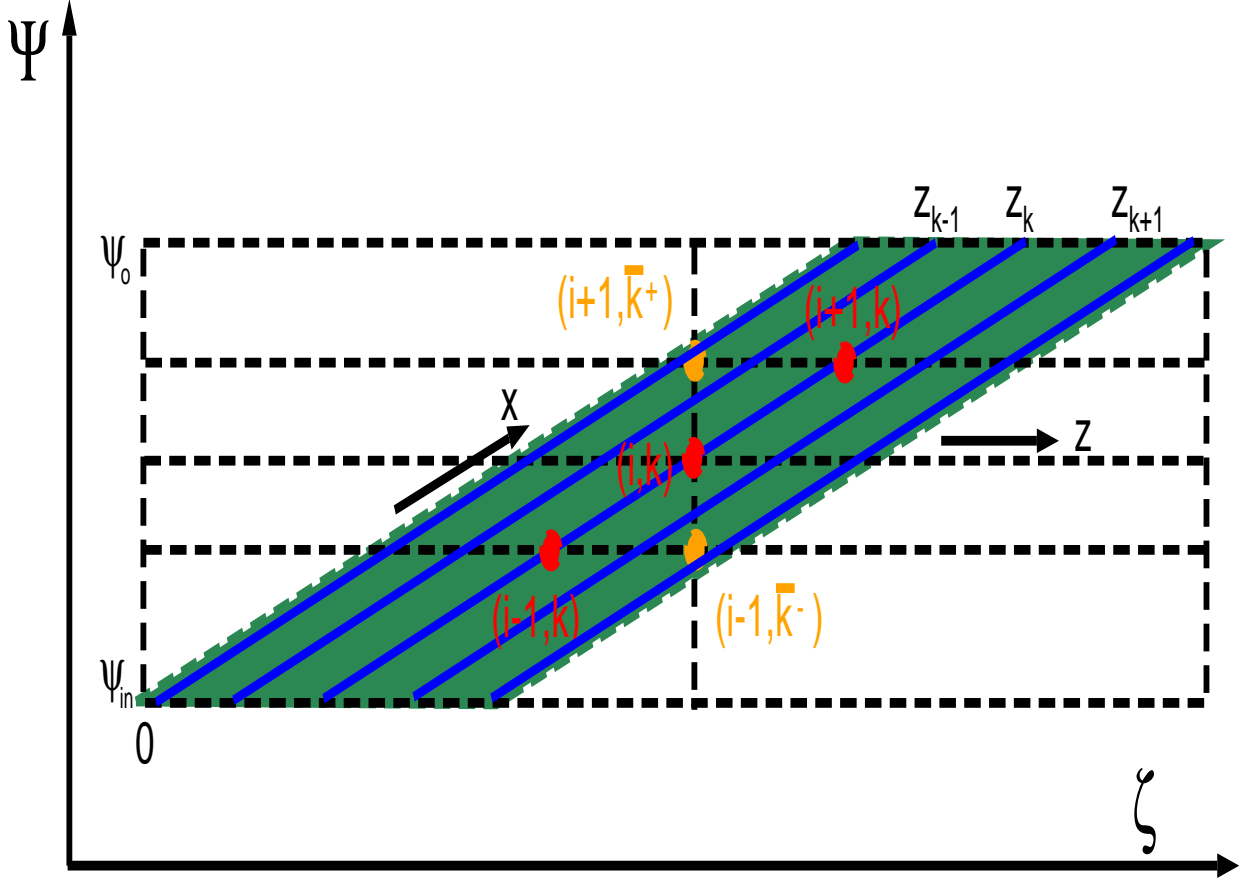


FIG. 3: A sketch of adjacent grid-points mapping from the field-aligned coordinates  $(x_{i-1}, y_j, z_k) \rightarrow (x_i, y_j, z_k) \rightarrow (x_{i+1}, y_j, z_k)$  to the usual flux surface coordinates  $(\psi_{i-1}, \theta_j, \zeta) \rightarrow (\psi_i, \theta_j, \zeta_k) \rightarrow (\psi_{i+1}, \theta_j, \zeta_k)$ .

### C. Numerical implementation of boundary conditions

#### 1. Toroidal ( $z$ ) boundary conditions

To ensure the toroidal periodicity, a full torus has to be divided into an integer  $\Delta n$  equal parts (toroidal wedges) and enforce periodicity on each of them.

$$F(x, y_k, z_{k+N}) = F(x, y_k, z_k), \quad (47)$$

$$z_{k+N} = z_k + L_z = z_k + N_z \Delta z, \quad (48)$$

where  $L_z$  is the toroidal length of the wedges,  $N_z$  is the number of nodal points, and  $\Delta z$  is the cell width.

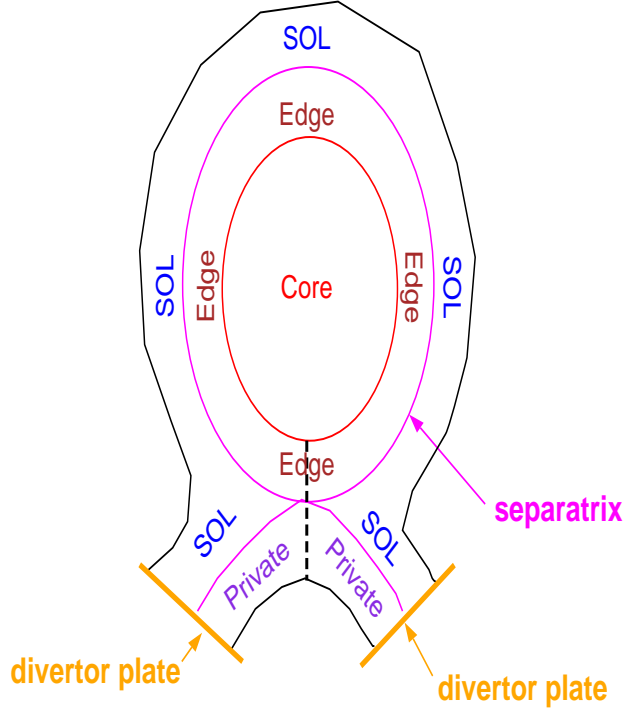


FIG. 4: The radial-poloidal plane is divided into three main regions: part of core (Edge), SOL, private flux region and divertor plates.

## 2. Parallel ( $y$ ) boundary conditions

The boundary conditions for  $\Phi$  is the sheath boundary conditions in  $y$  in the SOL and the private flux regions at the divertor plates, pseudo-periodic in  $y$  in “Edge” (the outer part of the closed flux region inside of separatrix), as shown in Fig. 4.

### • Twist-shift Edge boundary conditions

After one poloidal cycle along the field line, the end of the field line is shifted by a global pitch  $\oint \nu(\psi, \theta) dy$  in the binormal direction  $z$ , in general it may fall into a different but an identical toroidal wedge, so the poloidal periodicity must be enforced after each such cycle. A sketch of such procedures is pictorially shown in Fig. 5(a). The pseudo-periodic boundary conditions in a annular toroidal wedge then become:

$$F(x, y_{k+N}, \bar{z}_{k+N}) = F(x, y_k, z_k), \quad (49)$$

$$\bar{z}_{k+N} = \begin{cases} z_k - [\oint \nu(x, y) dy] \% L_z, & z_k > [\oint \nu(x, y) dy] \% L_z, \\ z_k - [\oint \nu(x, y) dy] \% L_z + L_z, & z_k < [\oint \nu(x, y) dy] \% L_z. \end{cases} \quad (50)$$

where the integral  $\oint \nu(x, y) dy$  represents a global shift by the periodicity constraint

in the field-aligning transformation. The symbol % represents the modulus operator, and the expression  $x\%y$  produces the remainder when  $x$  is divided by  $y$ , and thus is zero when  $y$  divides  $x$  exactly.

The consequence of these shifts is that there must be interpolation in  $z_k$  to the fact that the field-aligning transformation itself involves a shift and in general  $\hat{z}_k$  after the shift does not fall exactly on a nodal point in  $z_k$ . Therefore testing must be done to show that to which order of interpolation it makes no difference in the turbulence. Of course, finite Fourier transforms are exact up to machine accuracy. Using Lagrange interpolation scheme [40], we found that for a longest wavelength in z-direction, the 2-, 3-, 4-, and 5-points interpolation yield almost the same result, as shown in Fig. 5(b).

### • Sheath boundary conditions

An electrostatic sheath will form at any plasma boundary and acts to filter all but the high energy electrons while attracting ions, controlling the particle and energy flux leaving the plasma. Each ion-electron pair crossing the sheath convects to the surface a quantity of energy which is conventionally described using a total sheath heat transmission coefficient where [36]  $q_{se} = \gamma_e k T_e \Gamma_{se}$  with  $q_{se}$  total heat flux at the sheath edge,  $T_e$  the temperature,  $\Gamma_{se} \equiv N_i c_{se}$  the sheath edge particle flux and where

$$\gamma_e = 2.5 \frac{T_i}{T_e} + \frac{2}{1 - \delta_e} - 0.5 \ln \left[ \left( 2\pi \frac{m_e}{M_i} \right) \left( 1 + \frac{T_i}{T_e} \right) \frac{2}{(1 - \delta_e)^2} \right] \quad (51)$$

with  $\delta_e$  the secondary electron emission coefficient and  $T_i$  the ion temperature. Therefore in the SOL and private flux region, the divertor plate boundary conditions are

$$V_j = c_{se} = \sqrt{\frac{T_i + T_e}{M_j}} \quad (52)$$

$$j_{\parallel}^{el} = N_i e \left[ c_{se} - \frac{v_{Te}}{2\sqrt{\pi}} \exp \left( -\frac{e\phi}{T_e} \right) \right] \quad (53)$$

$$q_{se} = -\kappa_{\parallel e} \partial_{\parallel} T_e = \gamma_e N_i T_e c_{se} \quad (54)$$

$$g_{si} = -\kappa_{\parallel i} \partial_{\parallel} T_i = \gamma_i N_i T_i c_{se} \quad (55)$$

$$\partial_{\parallel} \varpi = 0 \quad (56)$$

$$\partial_{\parallel} N_i = 0 \quad (57)$$

where  $\gamma_i \simeq 2.5$  and  $\gamma_e \simeq 7$  are sheath energy transmission factors. Here we assume that a magnetic field is in the normal direction to the divertor plates. There is no

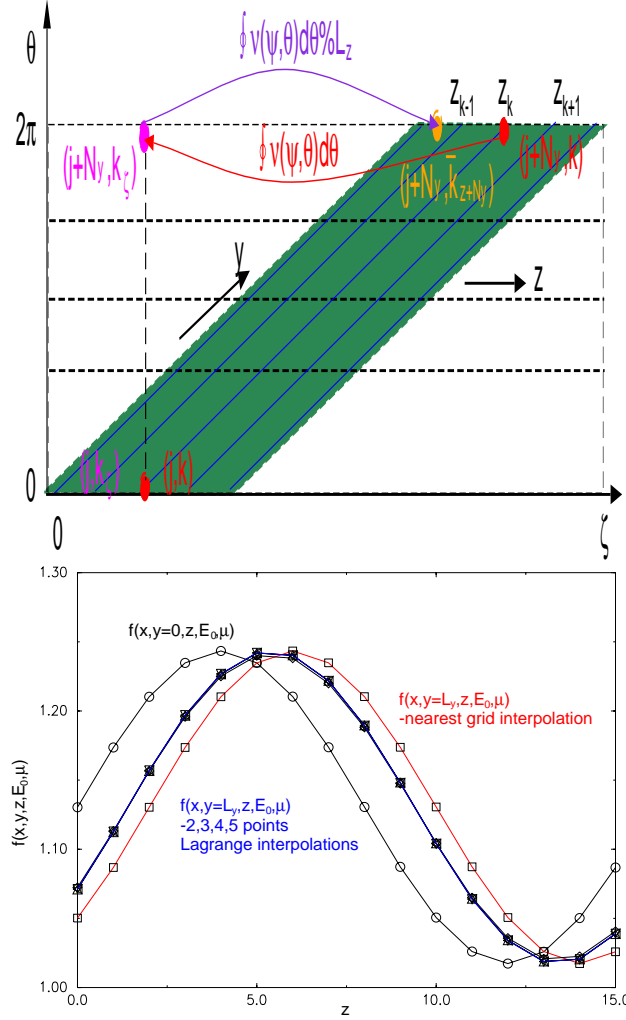


FIG. 5: (a) A sketch of poloidal periodic grid-points mapping from the field-aligned coordinates  $(x_i, y_j + 2\pi, \bar{z}_k) \rightarrow (x_i, y_j, z_k)$  to the usual flux surface coordinates  $(\psi, \theta_j + 2\pi, \zeta) \rightarrow (\psi_i, \theta_j, \zeta_k)$ , where  $\bar{z}_k = z_k - \oint \nu(\psi, \theta) d\theta$ ; (b) test results of twist-shifted periodic y-boundary using Lagrange interpolation scheme.

boundary condition for density  $N_i$  and vorticity  $\varpi$ . If a boundary condition has to be imposed for numerical reasons, the zero parallel gradient is used at the sheath entrance.



## V. SOLVING BOUT EQUATIONS WITH PVODE

The fluid equations in Sec. II solved by BOUT can be cast in the most general form in terms of a system of time-dependent ordinary differential equations (ODEs)

$$\frac{d\mathbf{u}}{dt} = \mathbf{f}(\mathbf{u}, \nabla\mathbf{u}, \nabla^2\mathbf{u}, \dots) \quad (58)$$

where  $\mathbf{u}$  is the vector of unknowns at a given mesh point, and  $\mathbf{f}$  is typically called right-hand-side function (rhs-f), which involves variables  $\mathbf{u}$  at a mesh point, and spatial derivatives of variables  $\mathbf{u}$  which are computed using finite difference. The rhs-f consequently depends upon the mesh point, its close neighbors, and difference schemes used.

BOUT code presently uses the Newton-Krylov approach. This scheme is exemplified by the BDF method (for Backward Differentiation Formula). For the BDF method, the advancement of  $\mathbf{u}$  from time level  $n - 1$  to  $n$  takes the form

$$\mathbf{u}_n = (\beta_1\mathbf{u}_{n-1} + \dots + \beta_k\mathbf{u}_{n-k}) + \Delta t\gamma_0\mathbf{f}_n \quad (59)$$

The BDF method is usually solved by a Newton iteration which expands  $\mathbf{f}_n$  at iteration  $j$  as

$$\mathbf{f}(\mathbf{u}^j) \approx \mathbf{f}(\mathbf{u}^{j-1}) + \frac{\partial\mathbf{f}}{\partial\mathbf{u}}(\mathbf{u}^j - \mathbf{u}^{j-1}). \quad (60)$$

Equation (59) then is a linear equation for  $\mathbf{u}_n^j$  which can be written as

$$(\mathbf{I}/\Delta t\gamma_0 - \mathbf{J})\mathbf{u}_n^j = \mathbf{g} \quad (61)$$

where  $\mathbf{I}$  is the identity matrix,  $\mathbf{J} \equiv \partial\mathbf{f}/\partial\mathbf{u}$  is the Jacobian evaluated with  $\mathbf{u}$  from a previous iteration or time step. Also,  $\mathbf{g}$  is a vector which depends on values of  $\mathbf{u}$  from the past iteration,  $\mathbf{u}^{j-1}$ , and at previous time steps as obtained from Eqs. (59-60). Equation (61) is usually solved by an iterative method to an accuracy somewhat better than the estimated error in  $\mathbf{u}_{n-1}$  from the time advancement; this is known as an inexact Newton method. We shall use a Krylov projection method to solve the linear system provided by a fully implicit solver: PVODE.[41, 42] Although more work is required for such Newton methods per iteration, they often have superior overall performance for stiff ODEs since larger time steps can be used. We compared two methods of advancing the equations in time: one is the Adams functional iteration (equivalent to predict-corrected method for a one-step functional iteration) and the second is the inexact Newton method utilizing matrix-free

Krylov projections as described. We found that the Newton-Krylov method is able to expand its time step by a factor of 70 in linear stage compared to the functional-iteration Adams method for the same accuracy [43]. However, it is only about six times more efficient due to the extra work required to expand the large time step. In the nonlinear stage of the simulation where different wave modes are strongly coupled, the Newton method reduces its time step by about 1/2 to satisfy the accuracy constraint. In fact, this simulation includes the shear in the magnetic equilibrium near the X-point which was a problem that we could not integrate successfully with the previous predictor-corrector method (a one-step functional iteration). Thus, using the Newton-Krylov method has become an essential part of our BOUT simulations.

Newton schemes that utilize a matrix-free Krylov projection method often require preconditioning. [41, 42] The procedure requires the ability to solve related linear systems  $\mathbf{P}\mathbf{v} = \mathbf{h}$  with a matrix  $\mathbf{P}$  which approximates the original matrix, but is simpler to solve. By assumption,  $\mathbf{P} \sim (\mathbf{I}/\Delta t\gamma_0 - \mathbf{J})$ . Noting that  $\mathbf{P}^{-1}\mathbf{P} = \mathbf{I}$ , we may insert this product into Eq. (61) to form the preconditioned system

$$[(\mathbf{I}/\Delta t\gamma_0 - \mathbf{J})\mathbf{P}^{-1}](\mathbf{P}\mathbf{u}_n^j) = \mathbf{g}. \quad (62)$$

The new variables are  $\mathbf{P}\mathbf{u}_n$ , and this system is easier to solve by iterative methods such as the Krylov method since  $[(\mathbf{I}/\Delta t\gamma_0 - \mathbf{J})\mathbf{P}^{-1}] \equiv \mathbf{A} \sim \mathbf{I}$  is more diagonally dominant. The Krylov method does require matrix-vector products of  $\mathbf{A}(\mathbf{P}\mathbf{u}_n)$ , and these are done in a matrix-free manner with a finite-difference quotient approximation  $\mathbf{J}\mathbf{v}$ . [41] However, we find that the implicit BOUT works well without a preconditioner, which may be related to the smaller time step required to resolve the turbulent fluctuations.

## VI. BOUT SOFTWARE DESIGN

To simulate boundary plasma turbulence and validate with the corresponding experiments, the BOUT code uses realistic X-point magnetic and plasma profiles. The background magnetic field structure is obtained from an MHD equilibrium code (usually EFIT [13]) for a typical shot. The plasma profiles are obtained by taking density and temperature as analytic fits (such as modified tanh) to Thomson scattering data or calculated from the edge transport code UEDGE [12]. For theoretical scaling studies with plasma current, the background

magnetic field structure is obtained from another MHD equilibrium code, Corsica [14]. For typical DIII-D boundary plasma profiles in L-mode, the midplane values on the magnetic separatrix are:  $T_e = 60\text{eV}$ ,  $T_i = 240\text{eV}$ , and  $n_i = 6.5 \times 10^{18}/\text{m}^3$ . From the given magnetic geometry and plasma profiles corresponding to a specific experimental device and discharge, the simulation is initialized with a set of small random fluctuations. The fastest growing modes dominate the initial phase of the calculation, in which the fluctuations grow at an approximately exponential rate. After this initial linear phase, the density and electrostatic potential fluctuations evolve to a saturated state with many modes. From the saturated steady state, turbulence statistical properties can be extracted from the BOUT simulations by using the correlation function analysis and validated with the various fluctuation measurements. [16, 17, 35, 44] The procedures of utilization of BOUT software suite is sketched in Fig. 6. Here EFIT and Corsica are MHD equilibrium codes for initial magnetic geometry setup for a whole device, UEDGE is an edge transport code for finer grid generation at the boundary region across the magnetic separatrix using spline and/or for plasma profiles. ELITE is a linear MHD stability code for peeling-ballooning modes [45] and BAL is a linear stability code for drift-wave-type instabilities [15] and lately 2DX [46] for BOUT benchmark studies, and GKV is a collection of IDL routines using the correlation function techniques for data analysis. Data from BOUT simulations are saved and later analyzed with the GKV and other BOUT data analysis IDL routines for post-processor to obtain fluctuation spectra, two-point correlation functions (including correlation times and lengths), bi-spectra, etc.

BOUT kernel code is a collection of subprograms that embodies physical or numerical functionalities, which includes but not limits to the following: grid generation, data allocation, initial conditions, boundary conditions, field-solve for vorticity and vector potential, rhs-f evaluation, and parallelization, and interface between the BOUT data and PVODE data (which advances a vector of variables  $\mathbf{u}$  using the Newton-Krylov method). The complete BOUT code description can be found in BOUT manual [47].

BOUT is parallelized via a poloidal domain decomposition model that uses the MPI (Message Passage Interface) system [11]. The parallel implementation is straightforward and efficient: one or several poloidal meshes with the entire radial-toroidal plane are stored on each processor. At the end of a time step, the data in the domain boundary planes are passed to its physically neighboring processor. Because of this parallel paradigm, the amount of message passing scales linearly with the problem size. For a typical run with 64 processors,

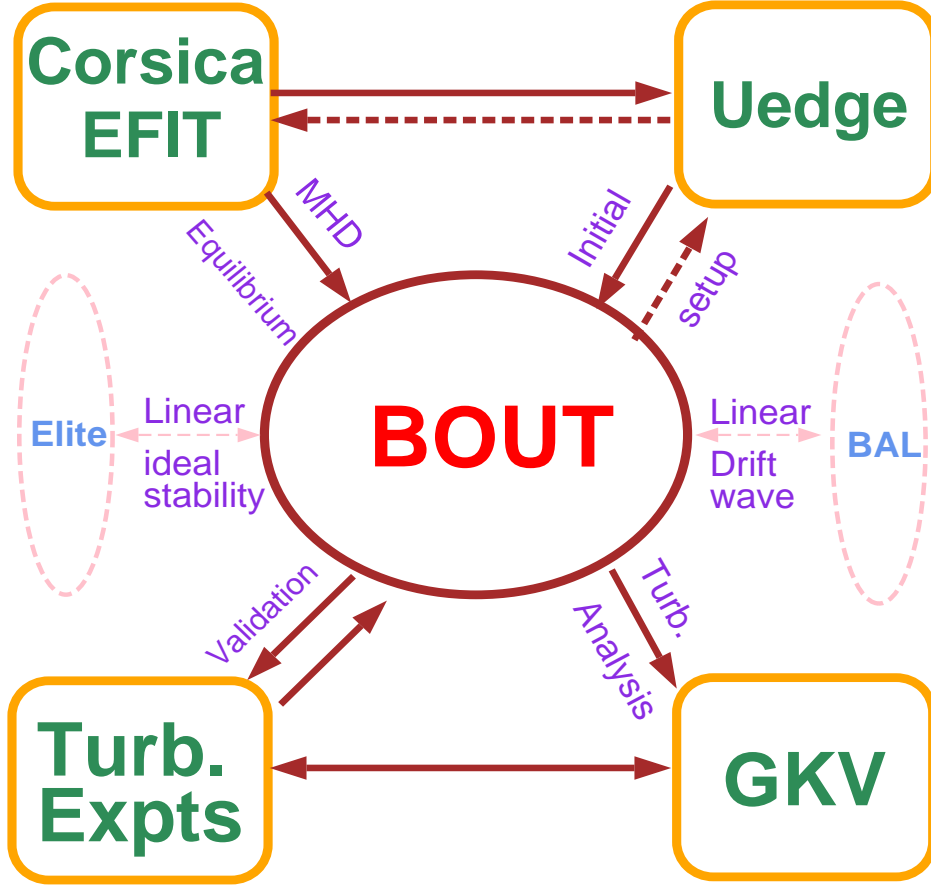


FIG. 6: BOUT software suite: a suite of the codes work together to make BOUT simulation results similar to real experiments.

the communication time is less than 1% [43].

## VII. BOUT SIMULATION RESULTS

BOUT is an electromagnetic fluid edge turbulence code [3, 9]. The physics model is based on the Braginskii equations for a collisional plasma, and the equations are solved numerically in the real geometry of a divertor tokamak. BOUT model supports a large variety of plasma modes: ideal and resistive ballooning and kink modes, drift, shear-Alfven, sheath-driven modes and others.

With such a complex numerical model two questions naturally arise: (i) whether the equations form a valid physics model for the studied phenomena, and (ii) whether the equations are solved correctly by the code. The answer to the first question is that for sufficiently

collisional plasma, which is reasonably well satisfied in many existing tokamaks, the collisional closure should hold and thus the model should be valid. To address the second question one needs to do thorough verification testing to make sure the numerical model can be trusted as a research tool. Four test problems have been benchmarked for verification of the BOUT code [26]: (1) Shear Alfvén wave; (2) Resistive drift instability; (3) Resistive interchange instability; (4) Axisymmetric benchmark with UEDGE. A suite of codes are under development to extend the verification studies, and it is a step toward the creation of accepted verification standards for edge turbulence codes. These include linearized and nonlocal (e. g. separatrix-spanning) modes in axisymmetric (realistic divertor) toroidal geometry. The suite consists of (i) an initial value approach using the BOUT 3D fluid turbulence code, here run with the nonlinear terms turned off, and (ii) a new linear eigenvalue code 2DX [46] for the boundary plasma.

In the following, two nonlinear BOUT simulation results are presented to demonstrate its capabilities and functionalities.

#### **A. Density effects on tokamak edge turbulence**

A series of BOUT simulations has been conducted to investigate the physical processes which limit the density in tokamak plasmas [48]. In this section, the plasma profiles are frozen, while they are evolved in section B. With poloidal flux,  $\psi$ , normalized to unity on the separatrix, we typically take the inner simulation boundary condition to be  $\psi_c = 0.9$  and the outer boundary at  $\psi_w = 1.1$ . The toroidal segment is typically one tenth of the torus with full poloidal cross section. The boundary conditions for turbulence variables are homogeneous Neumann at  $\psi = x_c$  and at  $\psi = x_w$ , sheath boundary conditions in  $y$  in the SOL and the private flux regions at the divertor plates, twist-shifted periodic in  $y$  in the closed flux region due to the choice of field-aligned coordinates, and periodic in  $z$ . However for the electrostatic potential with the toroidal mode number  $n=0$  component, the boundary conditions are homogeneous Neumann at  $x = x_c$  and Dirichlet at  $x = x_w$ . The computational mesh has 64 poloidal and 64 toroidal mesh points, and 50 radial points. The background magnetic field structure is obtained from an MHD equilibrium code (*e.g.*, EFIT [13]) for a typical discharge. The plasma profiles of density and electron temperature  $T_e$ , are analytic fits (modified tanh) to Thomson scattering data. For scaling studies with plasma density, the

plasma pressure is held constant. For scaling studies with plasma current, the background magnetic field structure is obtained from the MHD equilibrium code Corsica [14]. Since there is no unstable edge localized mode (ELM) for our base case (L-mode), there is also no ELM for the density scans. Furthermore, the current gradient driven modes are explicitly turned off in this paper to focus our efforts on the density effects [35].

Simulations of turbulence in tokamak boundary plasmas show that turbulent fluctuation levels and transport increase with collisionality. As the edge density increases and the temperature decreases, BOUT simulations show that the resistive X-point mode transitions to the resistive ballooning mode, perpendicular turbulent transport approaches and finally dominates parallel classical transport, leading to substantially reduced contact with divertor plates and the destruction of the  $\mathbf{E} \times \mathbf{B}$  edge shear layer; the region of high transport then extends inside the last closed magnetic flux surface. The full consequences of the large radial transport were assessed by a set of 2D UEDGE transport simulations with increasing outboard convective radial transport to mimic the BOUT results for increasing density. These simulations show that this transport can lead to an X-point MARFE when a fixed-fraction carbon impurity radiation is included [48]. BOUT further demonstrates that the current scaling appears on a plot of discharge current versus density as an abrupt increase in radial transport once  $\bar{n}_e/n_G > 1$ . All of these results indicate that rapid edge cooling due to large radial transport is a key physics element of the tokamak density limit. The simulation results are qualitatively consistent with experimental observations from C-mod and DIII-D [49, 50] and analytical analysis including perpendicular heat convection based on the blob heat transport model [51].

These simulations are qualitatively consistent with previous theory and simulations given by Rogers, Drake, and Zeiler (RDZ) [4], with the exception of the safety factor  $q$ -dependence in their  $\alpha_d$  scaling. The three sets of simulations are extrapolated to compare with RDZ theory and experiments, and to check whether a density limit boundary line is crossed, as the arrows indicate in Fig. 7. In what follows, the word “agree” or “disagree” is in a qualitative sense, i.e., the same trend. (1). For fixed  $q$ , current  $I_p$  and pressure  $P$ , an increase in density  $n_e$  leads to a fixed  $\alpha$  and a decrease in  $\alpha_d$ ,  $\alpha_d \propto \sqrt{\lambda_{mfp}^e} \propto 1/\sqrt{n_e}$ . In this case, the density-limit boundary is crossed, and RDZ theory, BOUT simulations and experiments agree. (2). For fixed  $q$ , temperatures  $T_e, T_i$  and density  $n_e$ , a decrease in current  $I_p$  leads to an increase in  $\alpha \approx 1/I_p^2$  and constant  $\alpha_d$ . In this case, the density limit boundary is crossed,

$$\alpha \equiv Rq^2 \frac{\partial \beta}{\partial r} \propto \frac{nT}{RL_n} \left( \frac{a^2}{I_p} \right)^2 \propto \frac{P}{I_p^2}$$

$$\alpha_d \equiv \frac{1}{2\pi q_a} \frac{(\lambda_{mfp}^{(e)})^{1/2}}{(RL_n)^{1/2}} \left( \frac{M_i}{8m_e} \right)^{1/4} \propto \frac{(\lambda_{mfp}^{(e)})^{1/2}}{q_a}$$

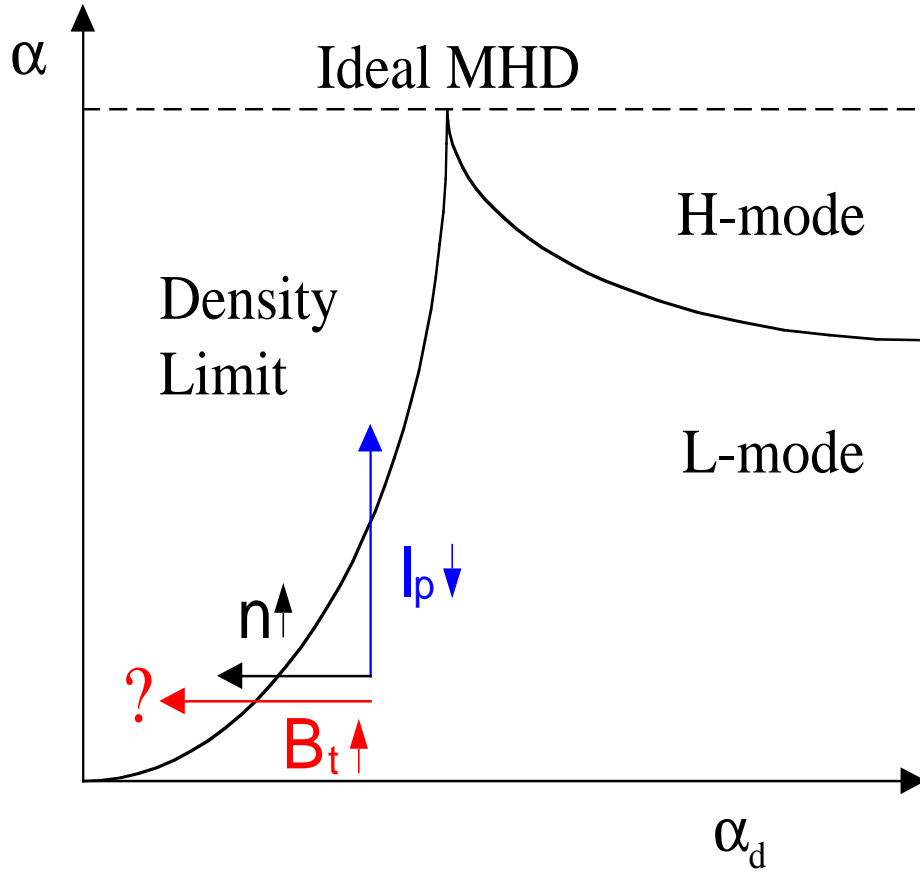


FIG. 7: A sketch of edge plasma phase space from Rogers, Drake, and Zeiler theory [4].

and RDZ theory, BOUT simulations and experiments agree. (3). For fixed  $I_p$ ,  $T_e$ ,  $T_i$  and  $n_e$ , an increase in toroidal magnetic field  $B_t$  leads to a fixed  $\alpha$  and a decrease in  $\alpha_d \approx 1/q$  since  $q \propto B_t$ . In this case, the RDZ theory predicts a density limit, but both experiments [52] and BOUT find no transition for this case. The disagreement may be due to two important pieces of physics omitted from RDZ theory that are kept in BOUT simulations: X-point physics

and SOL open-magnetic-field-line physics. X-point physics limits the mode to the outside midplane such that the parallel connection length  $qR$  is not a good measure of the parallel mode width because of  $q_a \rightarrow \infty$  near the magnetic separatrix in the divertor geometry. SOL physics contributes significantly to the formation of the  $E_r$  well and our simulations show that the onset of large radial transport is associated with the destruction of the  $E_r$  well [48].

## B. Blob dynamics and correlation analysis

For self-consistent turbulence and transport simulations with a neutral source added, as described in Sec. II C, we find that as density rises due to neutral fueling, turbulent transport increases. The same trend has been obtained with fixed plasma profiles as discussed in the previous section. The characteristics of the fluctuations also change from small scale turbulence to large density structures called blobs [53]. At high density during density ramp-up simulations, we have identified convective transport by localized plasma blobs in the SOL [19, 20, 54]. Such strong intermittent edge transport has been simulated previously in a 2D slab geometry [55].

An animation is given during density ramping, showing shear flow and blob dynamics (mpeg-1 video). A simple fluid neutral diffusion model is used where ion charge exchange (CX) gives rise to diffusion and ionization to the loss of neutrals. The neutral density at wall is  $N_w = 1 \times 10^{11} \text{cm}^{-3}$  and exponentially decays into the plasma. A poloidally nonuniform source of neutrals is specified with a peak around the X-point to mimic 2D neutral calculations, such as those in UEDGE. The detailed description of simulations is given in Ref. [58]. The animation clearly demonstrates that the turbulence originates inside the separatrix due to the steep density gradient. As density rises, the fluctuating density increases, the large-scale radial mode structure peels off near the separatrix due to poloidal shear flow, and isolated plasma blobs are therefore born. Plasma jets occasionally develop and remain connected to hot core plasma inside the separatrix.

The important properties include: (1) Blob detachment from the separatrix: spatially localized and non-diffusive transport of positive density fluctuations radially outward, as shown in Fig. 8(a). (2) Blob translation from dipole vorticity with the  $\mathbf{E} \times \mathbf{B}$  drift calculated from potential fluctuations, as shown in Fig. 8(b). The self-consistent E-field of the blob is predominantly a dipole field, increasingly as the blob moves away from the separatrix. The



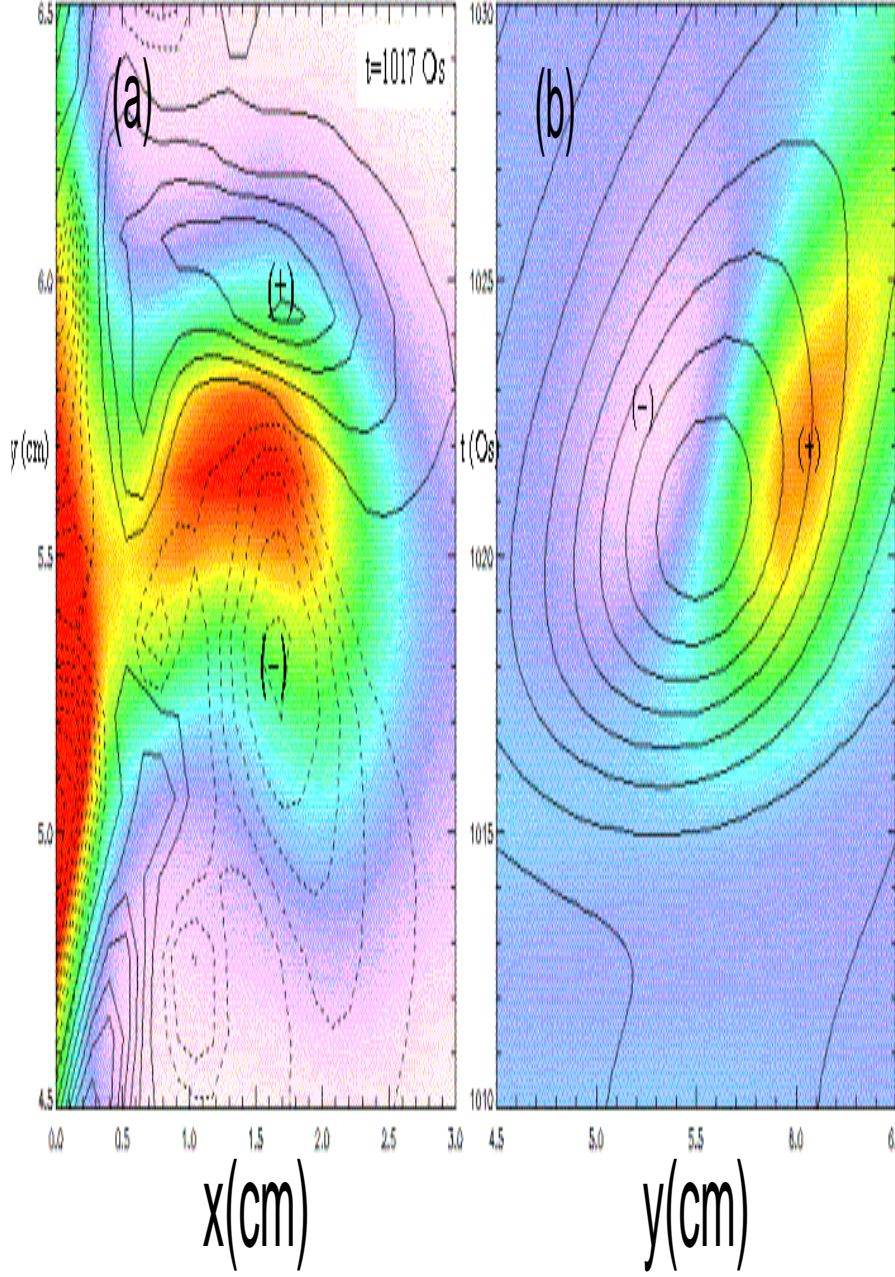


FIG. 8: (a) Blob detached from the separatrix, showing vorticity (contour lines) and density (color); (b) history of blob vorticity at the wall, density (contour lines) and vorticity (color).

radial velocity shows a weak variation with blob radius, as expected from “disconnected” blob models [19, 56]. (3) Blob rotation (monopole vorticity): observed to decay, probably due to  $T_e$  relaxation and/or sheath disconnection. (4) Cross correlation analysis indicates a decorrelation of turbulence between the midplane and the divertor leg due to strong X-point

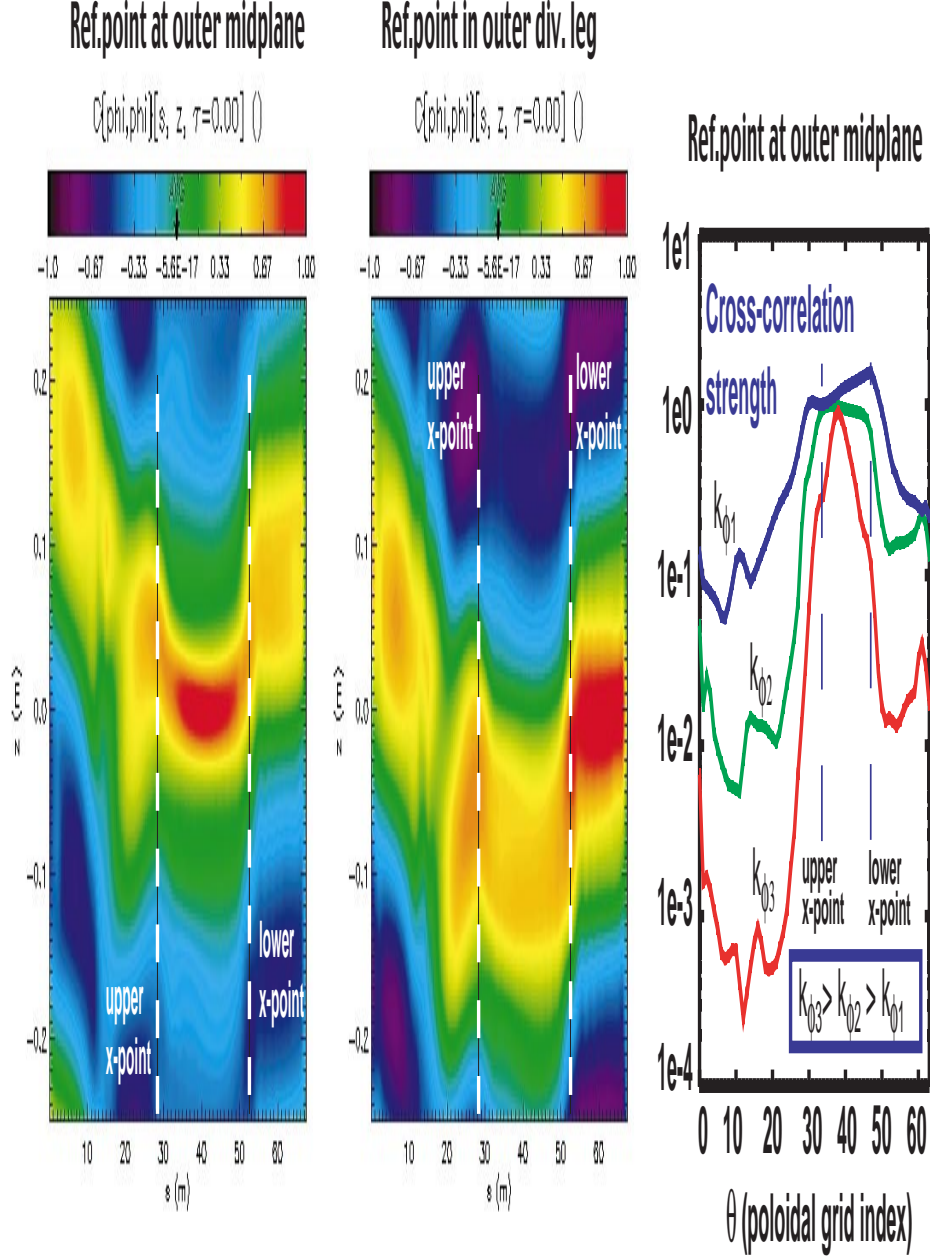


FIG. 9: (a) correlation function for reference point at outer midplane vs poloidal and parallel correlation length; (b) correlation function for reference point at outer divertor leg.

magnetic shear [57]. Figure 9(a) shows that the cross-correlation has cutoffs near both the lower X-point and the upper X-point regions for reference point at outer midplane, and the cutoff is more pronounced for larger poloidal wavenumber,  $k_{\theta}$ . Figure 9(b) shows that the cross-correlation has cutoffs near the X-point regions for reference point at outer divertor

leg. Figures 9(a) and 9(b) also show that the poloidal correlation length is about 1 cm, and the parallel correlation length is about 20 meters.

The simulation results also show the density buildup around the separatrix in L-mode during neutral fueling. The simulation data points with different neutral density at the wall and their fit to a “modified tanh fit” formula [58] are plotted in Fig. 10. The main effect of raising the neutral density (aside from raising the overall density) is to increase the density in the far SOL relative to the top of the density profile. The density gradient scale length parameters are obtained by fitting the modified tanhfit function to the profiles. There is a general overall trend for formation of a “knee” at the base of the profile and for the minimum density gradient scale length  $W_{data}$  to decrease with increasing density as observed in the experimental data [59]. However, the center position of the modified tanhfit (“knee” at the base of the profile) is moving toward the SOL and the modified tanhfit is no longer the best fit, due to the appearance of large blob structures as the density increases. The flat density profile in the SOL at high neutral density is a feature of convective transport by localized plasma blobs. The detailed blob dynamics for the case of neutral density  $N_n = 1 \times 10^{11} cm^{-3}$  in Fig. 10 is shown in Fig. 8, in the animation, and is analyzed in Ref. [19]. It is also found that the density gradient scale length at the separatrix  $W_{sep}$  is roughly constant with increasing density.

## VIII. SUMMARY AND CONCLUSIONS

It is shown in this paper that the application of a fluid model is, in many cases, reasonable in the boundary plasma of present fusion devices due to the low temperature and thus high collisionality. A unique boundary turbulence code, BOUT, has been developed that spans the separatrix, including three distinct regions: the outer part of the closed flux region (Edge), the SOL, and the private flux region. The field-aligned coordinates and annular toroidal wedge concept have been used for efficient simulations of the boundary turbulence. The detailed spatial numerical implementation has been presented. The innovative implicit Newton-Krylov iterative method is utilized via a fully implicit solver: PVODE. In order to simulate real experiments, BOUT is designed to couple to the edge plasma transport code UEDGE, and MHD equilibrium codes EFIT/Corsica to get the realistic X-point divertor magnetic geometry and plasma profiles. BOUT turbulence code suites offer unique and

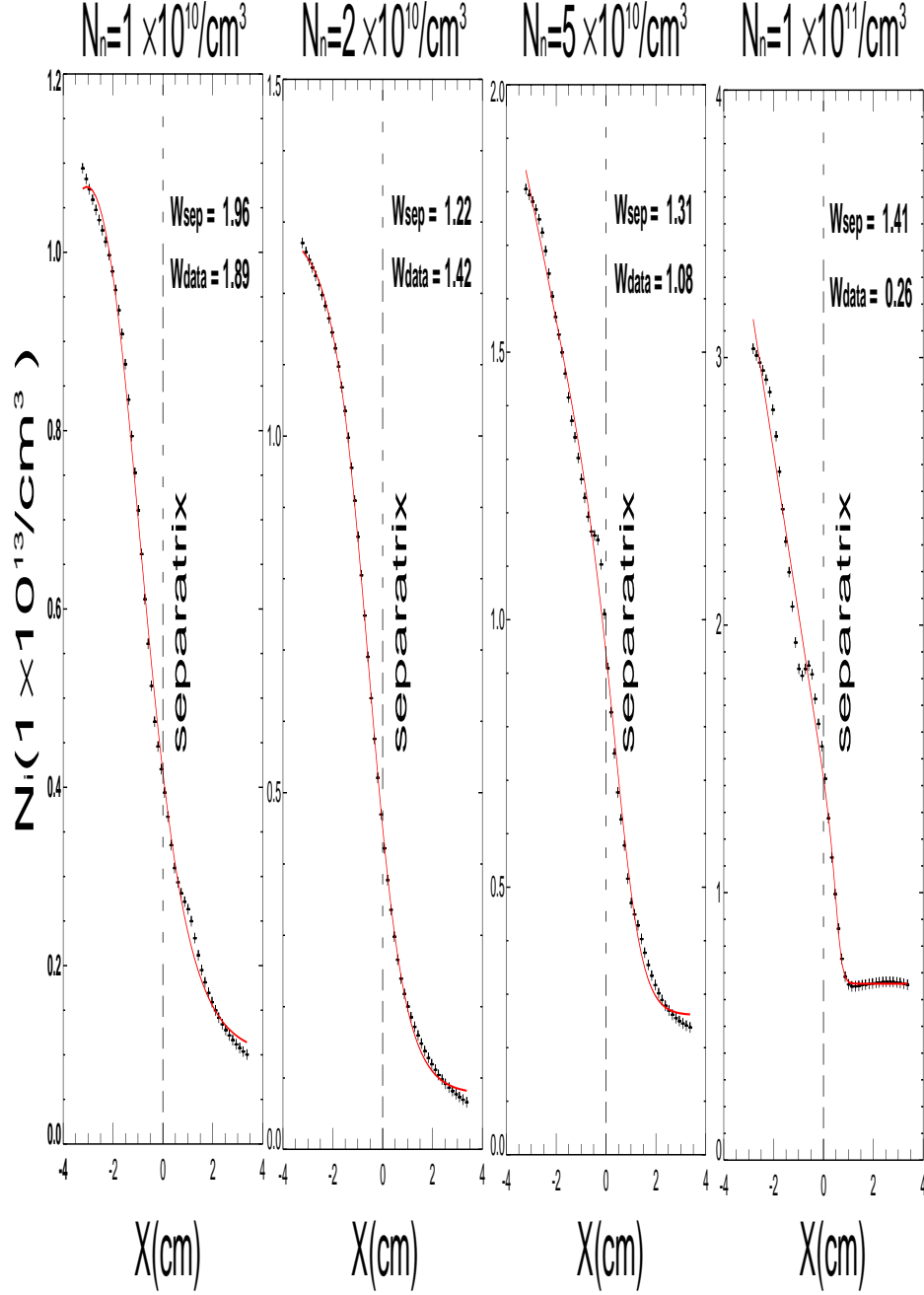


FIG. 10: Background plasma density and its modified tanh fit to the simulation profiles after  $\sim 0.5 - 1$  ms evolution vs. neutral density at the outside midplane

leading-edge numerical and computational resources that enable physical understanding for discovery, design and analysis.

We show that, in examples of BOUT simulation results, as density rises, the fluctuations change from resistive X-point mode to resistive ballooning mode dominated, and from small

scale turbulence to large blobs. In the large blob regime at high density, the enhanced radial transport as shown can lead to rapid edge cooling, which leads to a density limit. The description given here is consistent with recent experiments on C-Mod [49, 50] and analytical analysis including perpendicular heat convection based on the blob heat transport model [51]. BOUT simulations show that X-point effects can isolate blobs in the main SOL from divertor legs and also provide evidence of instability and fluctuations in divertor legs that is uncorrelated with activity in the main SOL. In summary, our results shed light on the qualitative trend and scalings, and provide suggestions of possible experimental control techniques.

## Acknowledgments

This work was performed under the auspices of the U.S. Department of Energy by Lawrence Livermore National Laboratory under Contract DE-AC52-07NA27344. We thank Drs. A. C. Hindmarsh, S. L. Lee, and A. Taylor for the PVODE support, R. H. Bulmer P. J. Catto, R. H. Cohen, A. M. Dimits, L. L. Lodestro J. R. Myra, W. H. Meyer W. M. Nevins, S. Krasheninnikov, L. D. Pearlstein G. D. Porter M. E. Rensink T. D. Rognlien, D. A. Russel D. D. Ryutov, and A. N. Simakov for fruitful physics discussions.

## 1. Differential operators

*a. Derivative along unperturbed magnetic field  $\vec{B}_0 \cdot \vec{\nabla}$*

$$\vec{B}_0 \cdot \vec{\nabla} A = (\vec{\nabla} z \times \vec{\nabla} x) \cdot (\vec{\nabla} y \frac{\partial A}{\partial y}) = \frac{1}{J} \frac{\partial A}{\partial y}. \quad (63)$$

*b. Laplacian  $\nabla_{\perp}^2$*

$$\nabla^2 A = \frac{1}{J} \sum_i \frac{\partial}{\partial x_i} \left[ J \left( \sum_j \frac{\partial A}{\partial x_j} \vec{\nabla} x_j \right) \cdot \vec{\nabla} x_i \right] \quad (64)$$

Neglecting  $\partial/\partial y$  terms, also dropping terms with first derivatives  $\partial A/\partial x$  and  $\partial A/\partial z$  that are small compared to those with second derivatives,

$$\nabla_{\perp}^2 A = |\vec{\nabla} z|^2 \frac{\partial^2 A}{\partial z^2} + 2(\vec{\nabla} z \cdot \vec{\nabla} x) \frac{\partial^2 A}{\partial z \partial x} + |\vec{\nabla} x|^2 \frac{\partial^2 A}{\partial x^2} \quad (65)$$

Then,

$$\nabla_{\perp}^2 A = (RB_{\theta})^2 \left( \frac{\partial^2 A}{\partial x^2} - 2I \frac{\partial^2 A}{\partial z \partial x} + \left[ I^2 + \frac{B^2}{(RB_{\theta})^4} \right] \frac{\partial^2 A}{\partial z^2} \right) \quad (66)$$

*c. Operator  $\vec{B} \times \vec{\nabla} \phi \cdot \vec{\nabla} A$*

$$V_E \cdot \vec{\nabla} A = \frac{c}{B^2} \vec{B} \times \vec{\nabla} \phi \cdot \vec{\nabla} A = c \left( \frac{\partial \phi}{\partial z} \frac{\partial A}{\partial x} - \frac{\partial \phi}{\partial x} \frac{\partial A}{\partial z} \right) \quad (67)$$

*d. Operator  $\tilde{b} \cdot \vec{\nabla} G$*

$$\tilde{b} \cdot \vec{\nabla} G = \vec{\nabla} A_{\parallel} \times \vec{B} \cdot \vec{\nabla} G = \frac{\partial A_{\parallel}}{\partial x} \frac{\partial G}{\partial z} - \frac{\partial A_{\parallel}}{\partial z} \frac{\partial G}{\partial x} \quad (68)$$

- 
- [1] M. Greenwald, M., J. J. Terry, *et al.*, Nucl. Fusion **28** (1988) 2199; M. Greenwald, Plasma Phys. Control. Fusion **44**, R27-R80(2002).
  - [2] S. J. Zweben, J. A. Boedo, O. Grulke, C. Hidalgo, B. LaBombard, R. J. Maqueda, P. Scarin and J. L. Terry, Plasma Phys. Control. Fusion **49** S1-S23(2007).
  - [3] Xu, X. Q., Cohen, R. H., Rognlien, T. D., and Myra, J. R., Phys. Plasmas, Vol. **7**, (2000) 1951.
  - [4] Rogers, B. N., and Drake, J. F., Phys. Rev. Lett. **81** (1998) 4396.
  - [5] B. Scott, Phys. Plasmas, Vol. **5**, 1845 (2001); Plasma Phys. Control. Fusion **49** S25S41 (2007).
  - [6] K. Hallatschek, Plasma Phys. Control. Fusion **49** B137B148(2007).
  - [7] P. Beyer, S. Benkadda, G. Fuhr-Chaudier, X. Garbet, Ph Ghendrih, and Y. Sarazin, Plasma Phys. Control. Fusion **49** 507523 (2007).
  - [8] V. Naulin, Journal of Nuclear Materials, V. **363-365**, 24-31 (2007); V. Naulin, T. Windisch, and O. Grulke, Physics of Plasmas, V. **15**, 012307 (2008).

- [9] X. Q. Xu, and R. H. Cohen., Contributions to Plasma Physics **38**, 158 (1998).
- [10] G. D. Byrne and A. C. Hindmarsh, Int. J. High Perf. Comput. Appl., Vol. **13**, (1999) 354-365.
- [11] W. D. Gropp, E. Lusk, and A. Skjellum, *Using MPI Portable Parallel Programming with the Message-Passing Interface*, The MIT Press, Cambridge, MA, 1994
- [12] T. D. Rognlien, D. D. Ryutov, N. Mattor, and G. D. Porter, Phys. Plasmas **6**, 1851 (1999);
- [13] LAO, L.L., ST. JOHN, H., *et al.* Nucl. Fusion **25** (1985) 1611.
- [14] PEARLSTEIN, L.D., *et al.* Proc. 28th EPS Conf. Controlled Fusion Plasma Phys, Madeira, Portugal, June 2001, (EPS, Funchal, 2001), Vol. 25A (ECA), p. 1901; <http://www.cfn.ist.utl.pt/EPS2001/fin/authors/nav/AutP01fr.html>
- [15] J. R. Myra, D.A. D'Ippolito, X.Q. Xu and R.H. Cohen, Phys. Plasmas **7**, 4622 (2000).
- [16] X. Q. XU, R. H. COHEN, W. M. NEVINS, *et al* , Nucl. Fusion, Vol. **42**, 21-27 (2002).
- [17] A. Mazurenko, M. Porkolab, D. Mossessian, and J. A. Snipes, X. Q. Xu and W. M. Nevins, PHYSICAL REVIEW LETTERS, VOL. **89**, 225004(2002)
- [18] G. R. McKee, R. J. Fonck, *et al*, Physics of Plasma , Vol. **10**, 1712-1719 (2003).
- [19] D. A. Russell, D. A. D'Ippolito, J. R. Myra, W. M. Nevins, and X. Q. Xu, PHYSICAL REVIEW LETTERS, VOL. **93**, 265001(2004).
- [20] D. A. Russell, J. R. Myra, and D. A. D'Ippolito, PHYSICS OF PLASMAS **14**, 102307(2007)
- [21] M. V. Umansky, ,T.D.Rognlien, X.Q.Xu, R.H.Cohen, and W. M. Nevins, Contributions to Plasma Physics , Vol. **44**, 182 - 187 (2004).
- [22] R. H. Cohen, *et al*, Nucl. Fusion **47** 612-625 (2007).
- [23] P. B. Snyder, H. R. Wilson and X. Q. Xu Phys. Plasmas **12** 056115 (2005).
- [24] M. E. Fenstermacher, T. H. Osborne, A. W. Leonard, P. B. Snyder, *et al*, NUCLEAR FUSION, VOL. **45**, (12): 1493-1502 DEC 2005.
- [25] J. H. Yu, J. A. Boedo, E. M. Hollmann, R. A. Moyer, D. L. Rudakov, and P. B. Snyder, Phys. Plasmas **15**, 032504 (2008).
- [26] M. V. Umansky, R. H. Cohen, L. L. LoDestro, and X. Q. Xu, Contrib. Plasma Phys. **48**, 2731 (2008).
- [27] B. Dudson, the 35th European Physical Society Conference on Plasma Physics, June 9-13 (35th EPS), Hersonissos, Crete, Greece.
- [28] T. D Rognlien, M. V. Umansky,X. Q. Xu, R. H. Cohen, L. L. LoDestro, Journal of Nuclear Materials, VOL. **337-339**, 327-331 (2005).

- [29] S. I. Braginskii, *Transport Properties in a Plasma*, in Review of Plasma Physics, MA Leontovich (ed.), Consultants Bureau, vol. 1, pp. 205-311 (1965).
  - [30] A. B. Mikhailovskii and V. S. Tsypin, Beitr. Plasmaphys. **24**, 335(1984), and references therein.
  - [31] A. N. Simakov and P. J. Catto, Physics of Plasmas, Vol. **10** (2003) 4744; Erratum: A. N. Simakov and P. J. Catto, Physics of Plasmas, Vol. **11** (2004) 2326.
  - [32] A. Zeiler, J. F. Drake, and B. N. Rogers, Physics of Plasmas Vol. **4** (1997) 2134.
  - [33] A. Zeiler, D. Biskamp, B. N. Rogers, and J. F. Drake, Physics of Plasmas Vol. **5** (1998) 2654.
  - [34] B. N. Rogers, and J. F. Drake, Physics of Plasmas Vol. **6** (1999) 2797.
  - [35] X. Q. Xu, W. M. Nevins, R. H. Cohen, J. R. Myra, and P. B. Snyder, New Journal of Physics **4**, 53.1-53.15 (2002).
  - [36] P. C. Stangeby *The plasma boundary of magnetic fusion devices* Institute of Physics Publishing, Bristol and Philadelphia, 2000.
  - [37] A. M. Dimits, Physical Review E **48** (1993) 4070.
  - [38] M. A. Beer, S. C. Cowley, and G. W. Hammet, Phys. Plasmas, Vol. **2**, 2687 (1995).
  - [39] B. Scott, Phys. Plasmas, Vol. **8**, 447 (2001).
  - [40] M. Abramowitz and I. A. Stegun, **Handbook of Mathematical Functions, National Bureau of Standards**, Applied Mathematics Series-55, Tenth Printing, December 1972.
  - [41] P. N. Brown and A. C. Hindmarsh, J. Appl. Math. Comp. **31**, 40 (1989).
  - [42] Y. Saad, Num. Lin. Alg. Applic. **1**, 387 (1994).
  - [43] T. D. ROGNLIEN, X. Q. Xu, and A. C. Hindmarsh, Journal of Computational Physics, **175**, 249-268 (2002).
  - [44] W. M. Nevins, X. Q. Xu, and T. N. Carlstrom, *et at.*, Proceedings of the 19th International Conference on Fusion Energy, Lyon, France, 14-19 October 2002, IAEA-CN-94/THP3/07.
  - [45] P. B. Snyder, H. R. Wilson, *et at.*, Phys. Plasmas **9** (2002) 2037; H. R. Wilson, P. B. Snyder, *et at.*, Phys. Plasmas **9** (2002) 1277.
  - [46] J. R. Myra and M. Umansky, Lodestar Report **#LRC-08-120**, April, 2008, <http://www.lodestar.com/LRCreports/Linear%20Analysis%20LRC%20Report.pdf>; the 35th European Physical Society Conference on Plasma Physics, June 9-13 (35th EPS), Hersonissos, Crete, Greece.
- J. R. Myra and M. V. Umansky, abstract of 2008 International Sherwood Fusion Theory



- Conference, March 30 - April 2, 2008, Boulder, Colorado, 2C8.
- [47] M. V. Umansky, X. Q. Xu, and B. Dudson, and L. L. Lodestro, BOUT code manual, LLNL, June, 2006. Available from [www.mfescience.org/bout/](http://www.mfescience.org/bout/).
  - [48] X. Q. Xu, W. M. Nevins, *et al.*, Phys. Plasmas **10** (2003) 1773.
  - [49] B. LaBombard, R. L. Boivin, M. Greenwald, *et al.*, Phys. Plasmas **8**, 2107(2001); B. LaBombard, J. W. Hughes, D. Mossessian, M. Greenwald, B. Lipshultz, J. L. Terry, *et al.*, Nucl. Fusion **45**, 1658 (2005).
  - [50] TERRY, J.L., ZWEBEN, S. J., *et al.*, Phys. Plasmas, **10**, 1739 (2003); Jerry, T. L., J. L. Terry, N. P. Basse, I. Cziegler, *et al.*, Nucl. Fusion **45**, 1321(2005).
  - [51] D. A. D'Ippolito and J. R. Myra, PHYSICS OF PLASMAS **13**, 062503(2006).
  - [52] PETRIE, T. W., KELLMAN, A. G., *et al.* Nucl. Fusion **33** (1993) 929.
  - [53] KRASHENINNIKOV, S.I., Phys. Lett. A **283** 368(2001).
  - [54] J. R. Myra and D. A. D'Ippolito, D. P. Stotler, S. J. Zweben, B. P. LeBlanc, and J. E. Menard, R. J. Maqueda, J. Boedo, PHYSICS OF PLASMAS **13**, 092509(2006).
  - [55] Sarazin Y. and Ghendrih P., Phys. Plasmas **5** 4214 (1998).
  - [56] D'IPPOLITO, D. A., MYRA, J. R., RUSSELL, D. A., *et al.*, 20th IAEA Fusion Energy Conference (Vilamoura, Portugal, 1-6 November 2004), IAEA-CN-116/TH/P6-2.
  - [57] UMANSKY, M.V.,*et al.*, Contr. Plasma Phys. **44**, 182(2004); J. Nucl. Mater., (2004).
  - [58] XU, X.Q., NEVINS, W.M., *et al.*, Contr. Plasma Phys. **44** (2004) 105.
  - [59] Groebner R. J. *et al.* 2002 19th IAEA FEC (Lyon, 2002) IAEA-CN-94/EX/C2-3.